TEST-ANCHORED VIBRATION RESPONSE PREDICTIONS FOR AN ACOUSTICALLY

ENERGIZED CURVED ORTHOGRID PANEL WITH MOUNTED COMPONENTS

Gregory P. Frady and Lowery D. Duvall
NASA Marshall Space Flight Center
Huntsville, Alabama

Clay W. G. Fulcher, Bruce T. Laverde and Ronald A. Hunt
ESTS Group, NASA Marshall Space Flight Center
Huntsville, Alabama

ABSTRACT

A rich body of vibroacoustic test data was recently generated at Marshall Space Flight Center for a curved orthogrid panel typical of launch vehicle skin structures. Several test article configurations were produced by adding component equipment of differing weights to the flight-like vehicle panel. The test data were used to anchor computational predictions of a variety of spatially distributed responses including acceleration, strain and component interface force. Transfer functions relating the responses to the input pressure field were generated from finite element based modal solutions and test-derived damping estimates. A diffuse acoustic field model was employed to describe the assumed correlation of phased input sound pressures across the energized panel. This application demonstrates the ability to quickly and accurately predict a variety of responses to acoustically energized skin panels with mounted components.

Favorable comparisons between the measured and predicted responses were established. The validated models were used to examine vibration response sensitivities to relevant modeling parameters such as pressure patch density, mesh density, weight of the mounted component and model form. Convergence metrics include spectral densities and cumulative root-mean squared (RMS) functions for acceleration, velocity, displacement, strain and interface force. Minimum frequencies for response convergence were established as well as recommendations for modeling techniques, particularly in the early stages of a component design when accurate structural vibration requirements are needed relatively quickly. The results were compared with long-established guidelines for modeling accuracy of component-loaded panels. A theoretical basis for the Response/Pressure Transfer Function (RPTF) approach provides insight into trends observed in the response predictions and confirmed in the test data.

The software modules developed for the RPTF method can be easily adapted for quick replacement of the diffuse acoustic field with other pressure field models; for example a turbulent boundary layer (TBL) model suitable for vehicle ascent. Wind tunnel tests have been proposed to anchor the predictions and provide new insight into modeling approaches for this type of environment.

Finally, component vibration environments for design were developed from the measured and predicted responses and compared with those derived from traditional techniques such as Barrett scaling methods for unloaded and component-loaded panels.

INTRODUCTION

Hardware design on a new launch vehicle (LV) program is subject to performance requirements, cost and schedule constraints, and manufacturing constraints. Design goals include low weight, healthy margins of safety and adequate performance, while satisfying cost, schedule, and manufacturing constraints. Although the design must meet the performance requirements and satisfy the constraints, neither experimental validation nor the analysis are so

constrained. Traditionally, hardware design has relied heavily on development and qualification testing programs. Within these programs, uncertainty exists due to issues such as unit-to-unit variability, boundary condition complexity and measurement error/bias. Often the test conditions do not fully represent the flight environment for practical reasons; this departure can result in overly conservative test specifications and less efficient designs.

Today, programs are becoming increasingly reliant on computational simulations that provide more information but substitute testing with modeling uncertainty. A promising trend is the migration of emphasis in test programs from hardware development toward experimental validation of the physics anchoring a computer simulation.

Accurate prediction of structural vibration response to broadband excitation of a fluid/structural panel interface is challenging. Added complexity arises when equipment of any significant weight is mounted to the vehicle panel. NASA has identified a need to standardize the approach for predicting broad-band response of mass-loaded panel assemblies. Standardization of any approach requires experimental validation in a controlled environment. The analysis methodology and experimental validation described in this paper are offered in the spirit of contributing toward that end.

A brief description of the test articles and ground test facility is provided. A flight-like vehicle panel was fabricated with various mounted equipment configurations for a range of mass-loaded panel assemblies. Validation of any approach that makes use of analytical models can be accomplished more readily if model fidelity is known to be adequate for the intended purpose. Modal surveys of the test hardware were performed for this purpose; data showing favorable modal correlation of the hardware and the finite element models (FEMs) developed for this study is provided.

In addition to model and methodology validation, evidence is supplied through convergence studies to evaluate the frequency range of interest for component interface forces and panel strains, parameters important to the design engineer. The convergence characteristics of these two design metrics were compared with local acceleration, velocity and displacement near the component mounts to determine which of the latter three provided the best indication of force and strain convergence.

One straightforward methodology for predicting response using a finite element approach is presented. Other related methodologies will be presented in a subsequent paper. Equations were developed using modal coordinates and are provided for use in frequency response analysis. The methodology was developed using the frequency response to a spatially correlated unit pressure field acting across the panel surface. The phasing of the applied forces depends on wave numbers of traveling pressure waves at the fluid/structure interface.
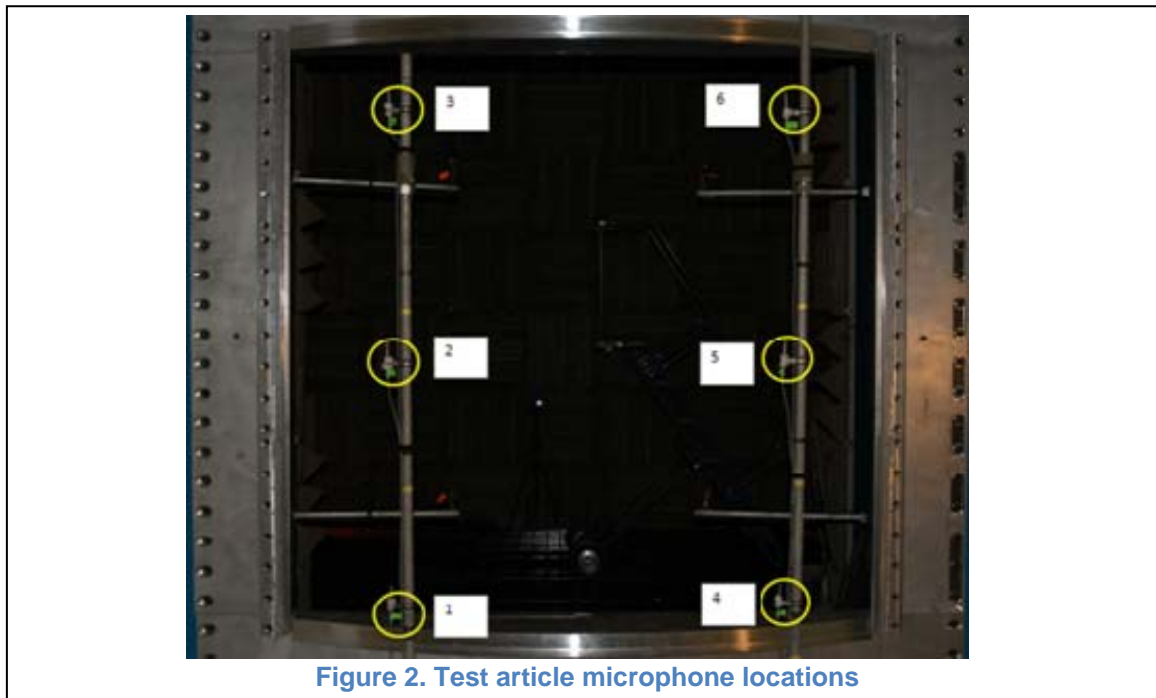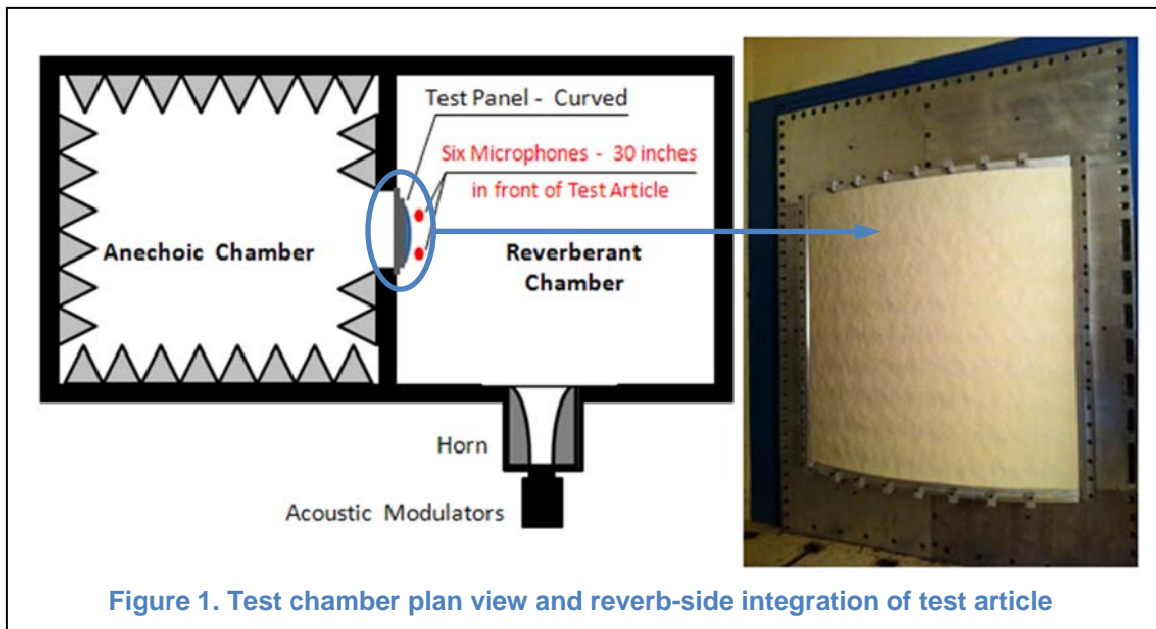
Several critical choices were made in the analysis to produce a convergent solution. To illustrate analytical convergence of the response, several parameter sensitivity studies were performed. The methodology includes a representation of the spatial correlation of a diffuse pressure field within the acceleration/pressure transfer function. Therefore, the effects of coincidence may be demonstrated in the response to any applied diffuse-field pressure. The sensitivity of the acceleration response to pressure patch density has proved to be an excellent way to illustrate the onset of coincidence effects on the vibratory responses.

EXPERIMENTAL HARDWARE AND TEST FACILITY

REVERBERANT TEST CHAMBER

Various configurations of a curved orthogrid panel assembly with representative component masses, designated "test articles," were acoustically loaded in a reverberant test chamber. Diffuse-field sound pressure levels (SPL) near the panel, and acceleration and strain responses on each panel assembly, were measured and recorded. Each test article was mounted to an opening in the wall separating the reverberant (source) and anechoic (receiver) rooms. The

test chamber is illustrated schematically in Figure 1, showing the source and receiver rooms, the test article, and the microphone sensor array. A photograph of a mounted panel as observed in the source room is also shown.

Figure 1. Test chamber plan view and reverb-side integration of test article

Figure 2. Test article microphone locations

The diffuse acoustic field was generated using conditioned air driven by four parallel WAS 3000 Modulators that fed sound into the room through a single horn. Sound pressures were monitored near the test article with six microphones, shown in the photograph of Figure 2. The

microphones were centered in six sectors and placed 30 inches in front of the test article. Several 1/3-octave band averaged spectra of the measured SPLs are presented in Figure 3. The SPL was designed to approximate the liftoff environment on a vehicle zone segment containing a typical instrument unit (IU) avionics panel. Environments typical of vehicle ascent in other zones were also tested, and these will be presented in a subsequent paper.

Although the acoustic response tests were conducted using four distinct sound pressure level (SPL) spectra, the results from just one of those fairly repeatable levels was simulated and discussed for this submission. In Figure 3, each curve represents the average of six measurements.

Figure 3. Measured acoustic spectra (corresponds to liftoff level)
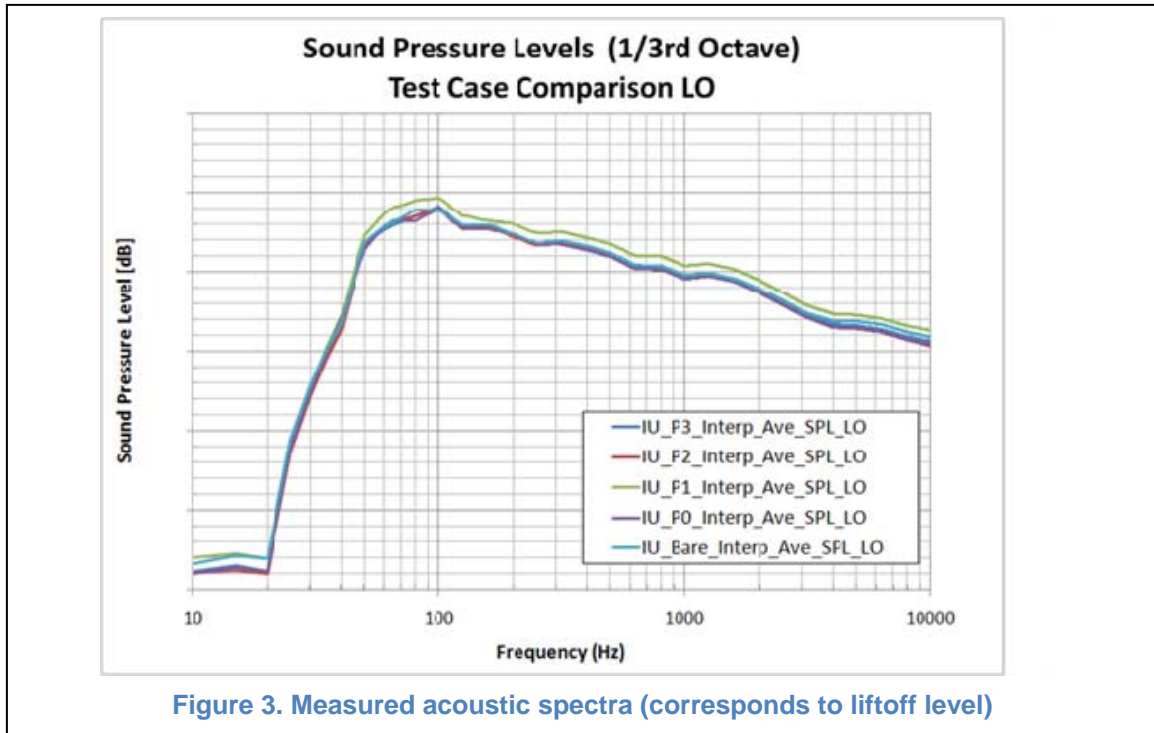
CURVED ORTHOGRID PANEL ASSEMBLY (TEST ARTICLE)

Major features of the assembled test article are shown in Figure 4. The curvature of the orthogrid panel spanned approximately 45° of a 216.5-inch diameter cylinder, typical of a launch vehicle (LV) skin. This representative section, 81 inches in height and fabricated from aluminum alloy, was configured for fastening to the dividing wall of the reverberant chamber. The panel was fastened with screws in a 3-inch band around the entire perimeter. The arc length of the panel in the direction of curvature was approximately 85 inches.

Centered on the orthogrid panel was an assembly of plates mounted on four brackets fastened to the panel at orthogrid junctions. The plate assembly represented the mass and flexibility of a component mounted to the panel skin. The design conveniently provided the ability to vary the weight of the mock component by adding or removing a number of increment plates mounted to the center of the primary plate. A total of three increment plates were fabricated, providing four weighted mockup configurations plus the unloaded (bare) panel without any mounted component. The nomenclature for the panel assembly configurations is listed in Table 1.

Table 1. Panel Assembly Configurations

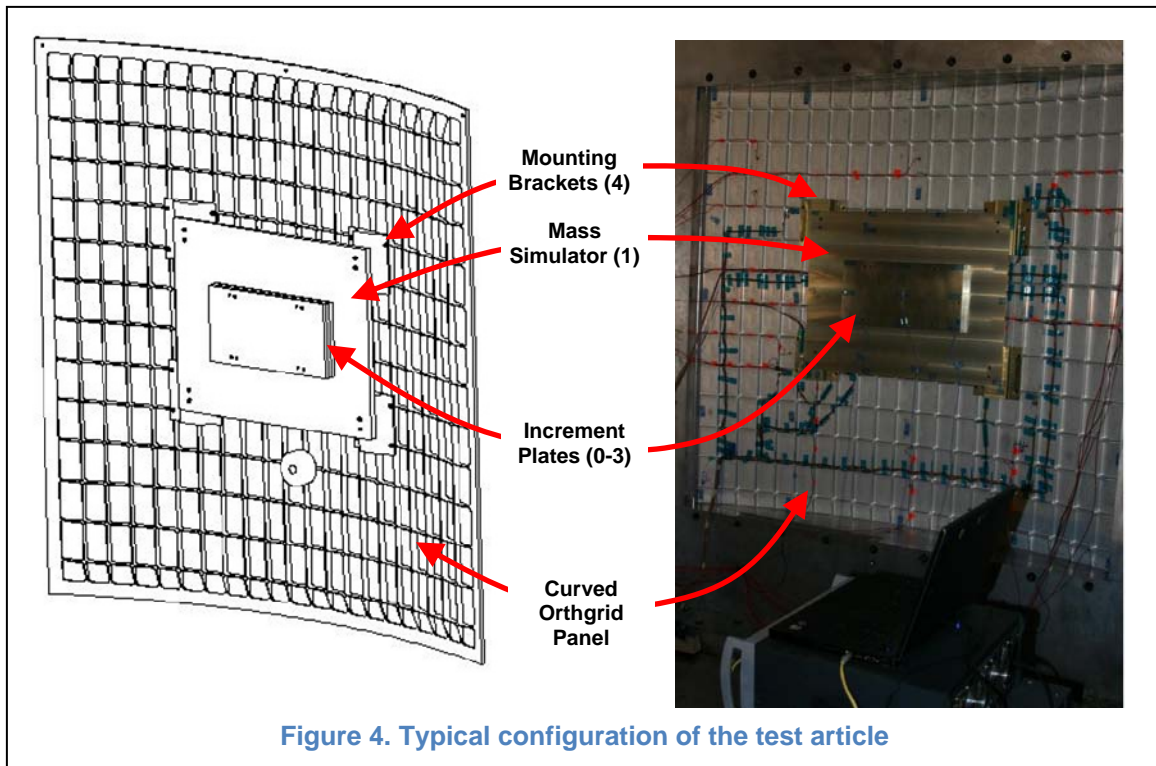| Configuration Name	Description	Primary Mockup Weight (lb)	Increment Plate Stack Weight (lb)	Total Component Weight (lb)
UL	Unloaded (Bare) Panel	0	0	0
W0	Panel + Primary	95.0	0	95.0
W1	Panel + Primary + 1 Incr Plate	95.0	15.4	110.4
W2	Panel + Primary + 2 Incr Plates	95.0	30.8	125.8
W3	Panel + Primary + 3 Incr Plates	95.0	46.2	141.2

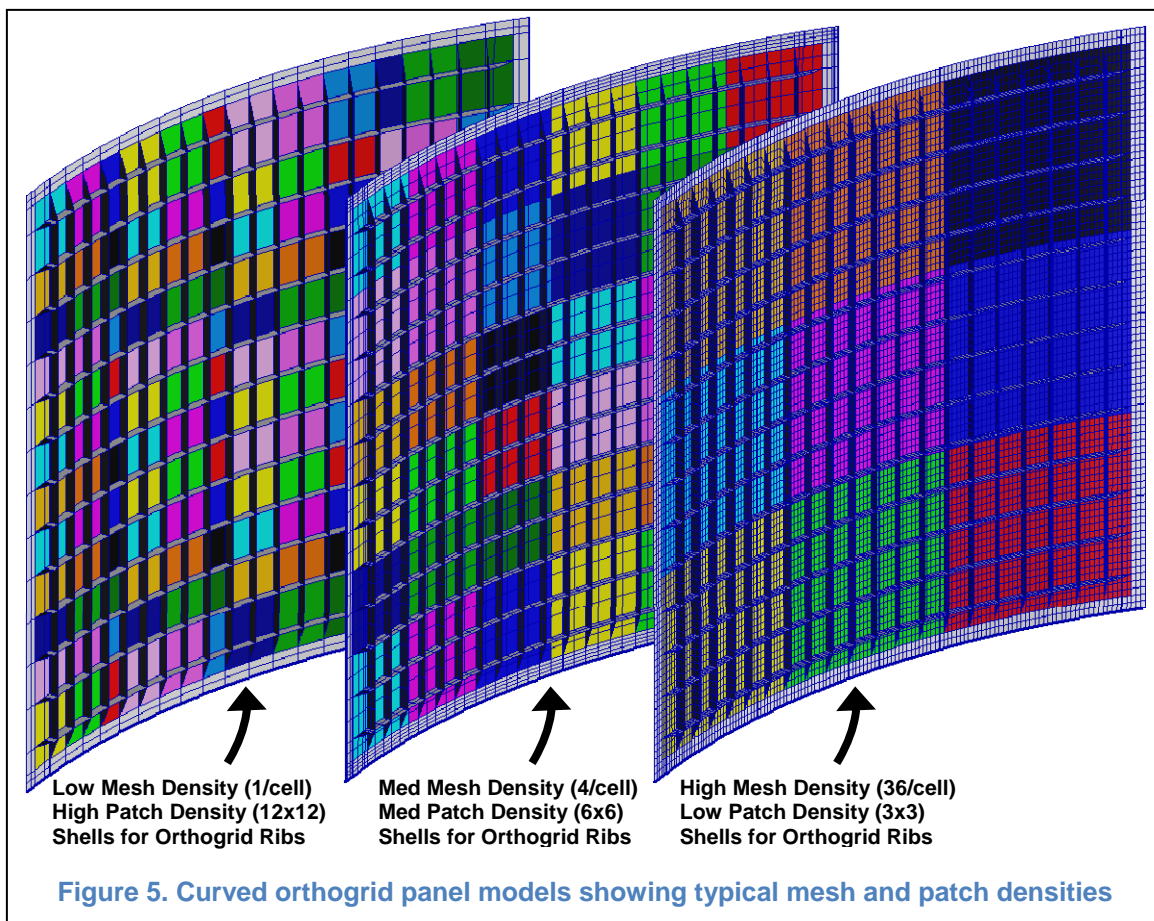**Figure 4. Typical configuration of the test article**

MODEL DESCRIPTION

CURVED ORTHOGRID PANEL FINITE ELEMENT MODEL

MSC/NASTRAN finite element models of the curved orthogrid panel and component mockups were developed [3]. Several versions of the panel model were designed to quantify response sensitivities to various parameters and model form, including mesh density and techniques for representing the ribs of the orthogrid panel. Several representative models of the bare panel are shown in Figure 5. Three mesh densities appear in the figure, ranging from low to high (1 - 36 CQUAD4 elements per orthogrid cell). Three methods were used to account for the additional panel mass and stiffness imparted by the orthogrid ribs: (a) explicit shell elements, (b) explicit beam elements, and (c) smeared composite shell properties for the panel elements (i.e., no explicit representation of the ribs).

The scheme for applying spatially correlated pressures over the test panel is also illustrated in Figure 5. Acoustic pressures were applied to "patches" of various sizes and approximately the same shape, representing regions of uniform applied pressure and illustrated in various colors. Since the size of the panel does not change, patch density may be considered

the total number of rectangular patches of approximately the same shape chosen for pressure application. For example a panel with two patches along each side would have a mesh density of 2x2=4 patches (per panel), and a panel with thirty patches along each side would have a mesh density of 30x30=900 patches (per panel). Response sensitivity to patch density is an important result of the simulations described in this submission.

In Figure 6, a typical component mockup is mounted to a panel through four bolted interface connections at the corners. Each corner bracket in the figure is mounted to the panel through four screws, with each screw connection represented by a 6 degree-of-freedom (DoF) CBUSH spring element connecting rigid RBE2 elements on either side of the spring. The footprint of the dependent degrees of freedom in each rigid element was chosen to approximate the preloaded region of the bolted connection. The bolt pattern between each bracket and a corner of the component plate was modeled in the same fashion. Thus, the total force and moment transmitted through each corner of the mockup were monitored through the bracket/component CBUSH element, and the forces in the four bracket screws at each corner were available if desired.

Low Mesh Density (1/cell)
High Patch Density (12x12)
Shells for Orthogrid Ribs

Med Mesh Density (4/cell)
Med Patch Density (6x6)
Shells for Orthogrid Ribs

High Mesh Density (36/cell)
Low Patch Density (3x3)
Shells for Orthogrid Ribs

Figure 5. Curved orthogrid panel models showing typical mesh and patch densities

In the acoustic tests, stacks of small stiff plates mounted near the center of the larger plate were used to vary the total weight of the component. Vibration test data from a series of five hardware configurations, including four weighted component/panel assemblies and the bare panel, allowed an assessment of response sensitivity to component weight. The increment stack weights were modeled with point mass elements (CONM2) attached with RBE2 rigid elements to the bolt locations of the larger plate, as illustrated in Figure 6.
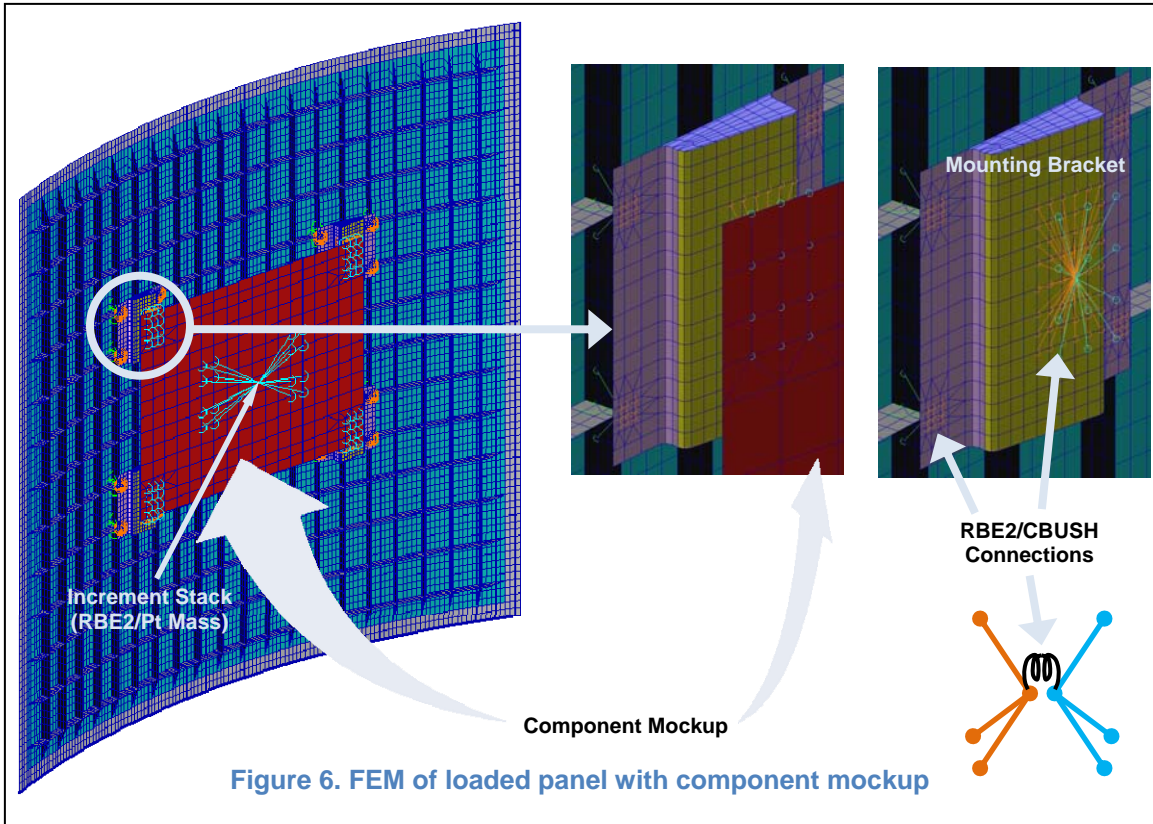
Figure 6. FEM of loaded panel with component mockup

Labels in figure: Increment Stack (RBE2/Pt Mass), Component Mockup, Mounting Bracket, RBE2/CBUSH Connections

Table 2. Designators for 1350 Model Variants (XX-EX-PXX-WX)

Placeholder (X)	Designation	Description			
XX	ES	Explicit Shell			
	EB	Explicit Beam			
	SC	"Smeared" Composite			
EX	1	1 x 1 = 1 Elements/Cell			
	2	2 x 2 = 4 Elements/Cell			
	6	6 x 6 = 36 Elements/Cell			
PXX	01	01 x 01 = 1 Patches/Panel			E1
	02	02 x 02 = 4 Patches/Panel		E2	
	⋮	⋮	E6		
	12	12 x 12 = 144 Patches/Panel			
	⋮	⋮			
	20	20 x 20 = 400 Patches/Panel			
	⋮	⋮			
	30	30 x 30 = 900 Patches/Panel			
WX	UL	Unloaded Panel (No Component)			
	0	Component with 0 Increment Plates, $\Delta W = 0$ (lb)			
	1	Component with 1 Increment Plate, $\Delta W = 15.4$ (lb)			
	2	Component with 2 Increment Plates, $\Delta W = 30.8$ (lb)			
	3	Component with 3 Increment Plates, $\Delta W = 46.2$ (lb)			

Designators for the complete family of models created for this study are summarized in Table 2. For example, the unique designator for panel model ES-E2-P20-W3 per Table 2 refers to a model that represents the orthogrid ribs as explicit shells (ES), a mesh density of 2 x 2 = 4 CQUAD4 elements per orthogrid cell (E2), a patch density of 20 x 20 = 400 patches (P20), and with the 46.2 lb increment stack (W3) attached. 885 model variants out of a theoretical maximum of 1350 were used in this study. Not all combinations of the configuration parameters in Table 2 are possible since the total number of patches is limited by mesh density. Also, no cases were assigned a patch density of 1. 885 model variants out of a theoretical maximum of 1350 were used in this study. Not all combinations of the configuration parameters in Table 2 are possible since the total number of patches is limited by mesh density. Also, no cases were assigned a patch density of 1.

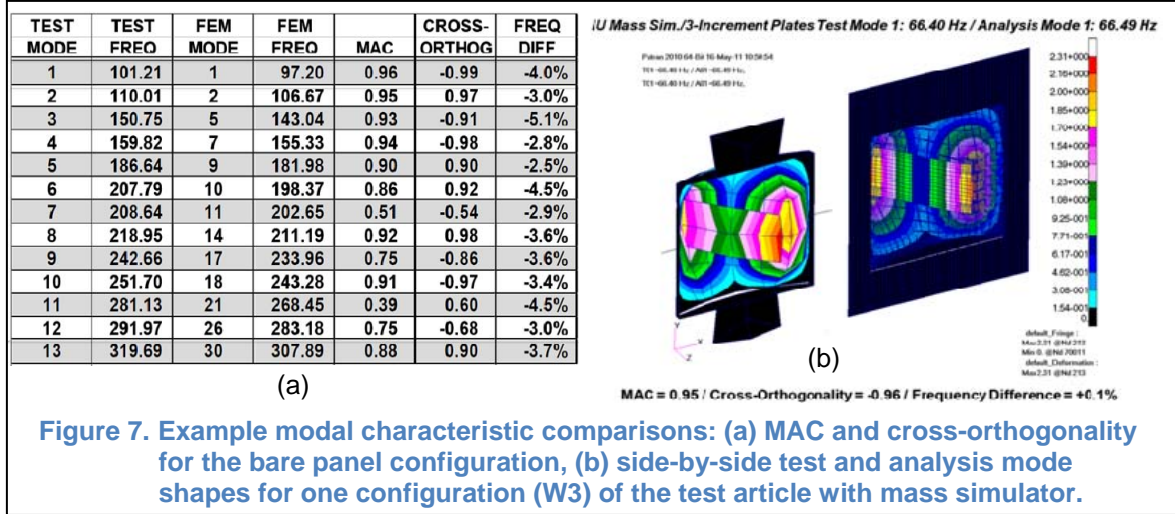## BOUNDARY CONDITIONS AND MODELING ASSUMPTIONS

The original FEMs developed for this program included detailed flexible representations of the chamber wall mount. To reduce the computational overhead required for thousands of response calculations, the boundary conditions were simplified by removing the flexible wall mount and locking the bolted perimeter to ground in six DoF. Minor deviations were observed in the panel assembly mode frequencies from this simplification, but did not significantly affect the results while gaining reasonable turnaround time in the numerous program runs required for the sensitivity analyses. Broad-band assignments of modal damping were manually chosen based upon overlays of the measured and analysis frequency responses. Damping of 1.0% - 2.0% of critical was used below 500 Hz, and 0.5% - 1.0% of critical above this frequency.

Flexibility of the interface joints between the panel and the component mounts, and the mounts and mockup components, was maintained by limiting the footprints of the rigid element connections to local groups of bolt locations. Although the increment plates were modeled as point masses, thus eliminating the flexibility of this component, this simplification was judged to be reasonable given the relatively high stiffness of the increment stack.

Finally, the input sound pressure field was assumed to be diffuse, and spatially correlated with a sinc function, described in detail later in this presentation [1].

MODAL SURVEY AND TEST/ANALYSIS CORRELATION

Comprehensive modal surveys of the test article assemblies were performed and have been reported in detail by [2]. Two examples of typically excellent test/analysis correlation, one for an unloaded panel and the other for the W3 configuration (mockup component with three increment plates) are presented in Figure 7. The correlation data was developed with a dense array of response points in a series of modal surveys: 32 tri-axial accelerometers (triax) for the empty fixture, 77 triaxes for the bare panel, and 85 triaxes for each of the mass-loaded panel configurations. The mode frequency and shape correspondence using the standard Modal Assurance Criterion (MAC), Cross-Orthogonality and qualitative mode shape depictions between the analytical and test results was observed to be excellent. Good correlation of the modal characteristics was not unexpected, as the test article and boundary conditions are straightforward to model. Since the modal survey work is secondary to the objectives of this paper, exhaustive results are not presented here.

TEST MODE	TEST FREQ	FEM MODE	FEM FREQ	MAC	CROSS-ORTHOG	FREQ DIFF
1	101.21	1	97.20	0.96	-0.99	-4.0%
2	110.01	2	106.67	0.95	0.97	-3.0%
3	150.75	5	143.04	0.93	-0.91	-5.1%
4	159.82	7	155.33	0.94	-0.98	-2.8%
5	186.64	9	181.98	0.90	0.90	-2.5%
6	207.79	10	198.37	0.86	0.92	-4.5%
7	208.64	11	202.65	0.51	-0.54	-2.9%
8	218.95	14	211.19	0.92	0.98	-3.6%
9	242.66	17	233.96	0.75	-0.86	-3.6%
10	251.70	18	243.28	0.91	-0.97	-3.4%
11	281.13	21	268.45	0.39	0.60	-4.5%
12	291.97	26	283.18	0.75	-0.68	-3.0%
13	319.69	30	307.89	0.88	0.90	-3.7%

(a)

(b)

MAC = 0.95 / Cross-Orthogonality = -0.96 / Frequency Difference = +0.1%

Figure 7. Example modal characteristic comparisons: (a) MAC and cross-orthogonality for the bare panel configuration, (b) side-by-side test and analysis mode shapes for one configuration (W3) of the test article with mass simulator.

UNIT PRESSURE APPLICATION

The FEMs were used to develop response/pressure transfer functions for applying measured sound pressure spectra. First, unit pressures on each patch were applied statically in NASTRAN with an OLOAD output request to determine the weighting factor on the six DoF forces on every node in the patch. Thus, a field of properly weighted nodal forces corresponding to unit pressure could be constructed for each patch. These forces were the basis for the patch response/pressure transfer functions developed in the next section. The application of measured sound pressures to the entire set of transfer functions resulted in the predicted acceleration, strain and interface force responses for comparing with measured data.

STRUCTURAL DYNAMICS ANALYSIS

A random pressure field on a launch vehicle skin surface may be approximated by dividing the surface into "patches," or regions of uniform pressure with zero phase. The size of each patch must be chosen small enough to justify the assumption of uniform (though dynamically varying) pressure with zero phase across the patch.

The pressure may be defined as a stationary Gaussian random field with spatially varying autospectral density. The pressures on any pair of patches may be correlated, exhibiting a non-zero cross-spectral density between them. The random pressure field is thus a square Hermitian matrix of spectral densities of dimension N_p, the total number of pressure patches. The pressure autospectra occur on the diagonal of the matrix. The cross-spectra appear off of the diagonal. The random pressure field on all patches may be written as

$$\boldsymbol{P}_{N_p}(\omega) = \begin{bmatrix} P_{11} & P_{12} & \cdots & P_{1N_p} \\ P_{21} & P_{22} & \cdots & P_{2N_p} \\ \vdots & \vdots & \ddots & \vdots \\ P_{N_p 1} & P_{N_p 2} & \cdots & P_{N_p N_p} \end{bmatrix} \qquad (1)$$

where $P_{bc} = P_{cb}^*$, and the asterisk denotes the conjugate operator. If spatial functions $\gamma(\omega, R)$ are defined that relate the autospectra to the cross-spectra, (1) may be written as

$$\boldsymbol{P}_{N_p}(\omega) = \begin{bmatrix} \gamma_{11}\hat{P}_{11} & \gamma_{12}\hat{P}_{12} & \cdots & \gamma_{1N_p}\hat{P}_{1N_p} \\ \gamma_{21}\hat{P}_{12} & \gamma_{22}\hat{P}_{22} & \cdots & \gamma_{2N_p}\hat{P}_{2N_p} \\ \vdots & \vdots & \ddots & \vdots \\ \gamma_{N_p1}\hat{P}_{1N_p} & \gamma_{N_p2}\hat{P}_{2N_p} & \cdots & \gamma_{N_pN_p}\hat{P}_{N_pN_p} \end{bmatrix} \tag{2}$$

where $\hat{P}_{bc} = \sqrt{P_{bb}P_{cc}}$ and γ_{bb} have been added to the diagonals for generalization. The expression for $\hat{P}_{bc}$ arises from an inequality requirement on the coherence which states that

$$0 \le \frac{|P_{bc}(\omega)|^2}{P_{bb}(\omega)P_{cc}(\omega)} \le 1.0 \tag{3}$$

For a diffuse field, the spatial functions γ may be expressed as

$$\gamma_{bc}(\omega, R_{bc}) = \frac{\sin\left(R_{bc}\,\kappa(\omega)\right)}{R_{bc}\,\kappa(\omega)} \tag{4}$$

where R_{bc} is the distance between the area centroids of patches b and c, $\kappa(\omega) = \omega/C_o$, and C_o is the speed of sound through the fluid medium adjacent to the patch material [1]. The patch area centroids are constrained to lie on the curved skin surfaces. When $b = c$, the spatial functions coincide with the patch autospectra, the distance R between patches vanishes and $\gamma_{bb} \to 1.0$ in the limit as $R_{bb} \to 0$ (L'Hopital's Rule). Finally, the patch autospectra may be expressed as products of frequency-dependent scaling functions $W_{bb}(\omega)$ and an arbitrary reference autospectrum. (e.g., one of the patch autospectra could be selected, but this is not required.)

$$P_{bb}(\omega) = W_{bb}(\omega)P_{ref}(\omega) \tag{5}$$

Substituting (5) into (2) we obtain an expression for the diffuse-field pressure model used for the simulated lift-off environments in this study:

$$\boldsymbol{P}_{N_p}(\omega) = \begin{bmatrix} \gamma_{11}W_{11} & \gamma_{12}W_{12} & \cdots & \gamma_{1N_p}W_{1N_p} \\ \gamma_{12}W_{12} & \gamma_{22}W_{22} & \cdots & \gamma_{2N_p}W_{2N_p} \\ \vdots & \vdots & \ddots & \vdots \\ \gamma_{1N_p}W_{1N_p} & \gamma_{2N_p}W_{2N_p} & \cdots & \gamma_{N_pN_p}W_{N_pN_p} \end{bmatrix} P_{ref} \tag{6}$$

where $W_{bc}(\omega) = \sqrt{W_{bb}(\omega)\,W_{cc}(\omega)}$. It is important to recognize that all of the pressure auto and cross-spectra represented in eqs (1) – (6) are known, and are related to the reference spectrum P_{ref} through the scaling functions. If the scaling functions are unknown, then the skin structure under consideration must be limited to regions with similar pressure autospectra and W_{bb} must

be set to unity. The scaling functions may also be grouped into fewer distinct sets for large regions showing uniform pressure autospectra. That is, many of the functions may be assigned the same value for various zones of the launch vehicle even if the zone is subdivided into many patches.

Now consider the acceleration frequency response $a_u(\omega)$ at a point j on the skin to a unit oscillating pressure $p_u(\omega) = \cos(\omega t)$ on patch b. The frequency response is also the transfer function between any acceleration response $a_j(\omega)$ at j to arbitrary pressure $p_b(\omega)$ on patch b. Note that the response point locations are unrestricted; they may be located either within or external to the patch. In NASTRAN, the unit pressure is distributed as a set of non-uniform forces on the nodes comprising the shell elements within the patch. This non-uniform force distribution for a unit pressure may be obtained with an OLOAD request at the patch nodes in NASTRAN SOL 101. The force distribution may then be swept through the frequency range of interest to obtain the frequency response. The acceleration/pressure transfer function for a single patch may be expressed explicitly as the sum of weighted acceleration/force transfer functions. The weighting factor is the static force F_k at each input location k on the patch due to a unit pressure (from an OLOAD request in SOL 101) [5]:

$$H_{a_j / p_b}(\omega) = \sum_{k=1}^{N_b} \left\{ F_k \cdot \sum_{m=1}^{M} \left[\frac{-\omega^2 \, \phi_{jm} \, \phi_{km}}{\omega_m^2 - \omega^2 + i \, 2 \zeta_m \, \omega_m \, \omega} \right] \right\} \tag{7}$$

where

$H_{a_j / p_b}(\omega)$ is the transfer function between acceleration at point j and pressure p_b on patch b,

F_k is the static force at point k associated with a unit pressure on patch b,

ϕ_{jm} is the mth mass-normalized mode shape at response point j,

ϕ_{km} is the mth mass-normalized mode shape at point k in the pressure patch,

ω is the circular frequency,

ω_m is the circular natural frequency of mode m,

ζ_m is the critical damping ratio for mode m,

N_b is the number of GRIDs in the pressure patch,

M is the number of retained modes.

The acceleration PSD response $A_{jb}(\omega)$ to a random pressure $P_{bb}(\omega)$ on patch b is the squared magnitude of the acceleration/pressure transfer function in (7) multiplied by the pressure PSD, or

$$A_{jb}(\omega) = \left| H_{a_j / p_b}(\omega) \right|^2 P_{bb}(\omega)$$
$$= \left| H_{a_j / p_b}(\omega) \right|^2 W_{bb}(\omega) P_{ref} \tag{8}$$

The total response at location j includes the autospectra from the pressures on all of the patches and also from non-zero cross-spectra between any two patches, or

$$A_j(\omega) = \sum_b^{N_p} \left| H_{a_j/p_b} \right|^2 P_{bb} + \sum_b^{N_p} \sum_{c \neq b}^{N_p} H_{a_j/p_b}^* H_{a_j/p_c} P_{bc}$$

$$= \sum_b^{N_p} \sum_c^{N_p} H_{a_j/p_b}^* H_{a_j/p_c} P_{bc} \tag{9}$$

Expressing eq (9) in terms of the reference spectrum and the spatially dependent cross-spectra of eqs (4) and (6), we obtain

$$A_j(\omega) = \sum_b^{N_p} \sum_c^{N_p} \gamma_{bc} W_{bc} H_{a_j/p_b}^* H_{a_j/p_c} P_{ref}$$

$$= \sum_b^{N_p} \sum_c^{N_p} \frac{\sin(\kappa R_{bc})}{\kappa R_{bc}} \sqrt{W_{bb} W_{cc}} H_{a_j/p_b}^* H_{a_j/p_c} P_{ref} \tag{10}$$

Note that the spatial functions γ reduce to unity for $b = c$, as mentioned previously. Eq (10) may be expressed in matrix form for computational efficiency in Matlab as [4]

$$A_j(\omega) = \left[\mathrm{H}_{a_j} \sqrt{\mathrm{W}} \; \Gamma \sqrt{\mathrm{W}} \; \mathrm{H}_{a_j}^\dagger \right] P_{ref} \tag{11}$$

where † denotes the Hermitian conjugate and

$$\mathrm{H}_{a_j}(\omega) = \left[H_{a_j/p_1} \quad H_{a_j/p_2} \quad \cdots \quad H_{a_j/p_{N_p}} \right] \quad \text{(a/p transfer functions from eq (7))},$$

$$\mathrm{W}(\omega) = \begin{bmatrix} W_{11} & & & 0 \\ & W_{22} & & \\ & & \ddots & \\ 0 & & & W_{N_p N_p} \end{bmatrix} \quad \text{(pressure autospectra scaling functions from eq (5))},$$

$$\Gamma(\omega) = \begin{bmatrix} 1 & \dfrac{\sin(\kappa R_{12})}{\kappa R_{12}} & \cdots & \dfrac{\sin(\kappa R_{1N_p})}{\kappa R_{1N_p}} \\ & 1 & \cdots & \dfrac{\sin(\kappa R_{2N_p})}{\kappa R_{2N_p}} \\ & \text{SYM} & \ddots & \vdots \\ & & & 1 \end{bmatrix} \quad \text{(spatial functions from eq (4))}.$$

If the pressure autospectrum does not vary significantly over the region of interest, $W_{bb}(\omega) = W_{cc}(\omega) \cong 1.0$, and eq (11) simplifies to

$$A_j(\omega) = \left[\mathrm{H}_{a_j} \; \Gamma \; \mathrm{H}_{a_j}^\dagger \right] P_{ref} \tag{12}$$

The term inside the bracket in eq (11) (or eq (12) for uniform pressure spectra) may be considered the squared transfer function between the total response at location j and the entire diffuse pressure field:

$$\left| H_{a_j/p}(\omega) \right|^2 = \mathrm{H}_{a_j} \sqrt{\mathbf{W}} \ \Gamma \sqrt{\mathbf{W}} \ \mathrm{H}_{a_j}^\dagger = \frac{A_j(\omega)}{P_{ref}(\omega)} \tag{13}$$

Note that $H_{a_j/p}$ is not an unchanging characteristic of the system since the scaling functions $\mathbf{W}$ depend upon the generally non-uniform patch autospectra which change at different points in the launch trajectory. However, if the random pressure may be considered uniform over the surface of interest, $H_{a_j/p}$ is characteristic of the system independent of input pressure or the output acceleration.

Eq (13) may be used to calculate $A_j(\omega)$ if the reference pressure P_{ref} and scaling functions $\mathbf{W}$ are known. Conversely, an effective reference pressure $\overline{P}_{ref}(\omega)$ may be calculated if the acceleration PSD is specified and $\mathbf{W}$ is set to the identity matrix. The locations j selected as reference points on a skin without mounted components should be few, and chosen as far as possible from zone boundaries, joints, or local skin features such as cutouts, or doublers.

Force and moment responses at specified interface elements (e.g., CBUSH) may be obtained in the same fashion by replacing the first mode shape term in (7) with the modal forces and moments obtained in any general purpose finite element code such as NASTRAN (SOL 103). The $-\omega^2$ term in the numerator of eq (7) is also dropped. Thus the force/pressure transfer function at interface location q for pressure on a single patch b is given by

$$H_{f_q/p_b}(\omega) = \sum_{k=1}^{N_b} \left\{ F_k \cdot \sum_{m=1}^{M} \left[\frac{\psi_{qm} \phi_{km}}{\omega_m^2 - \omega^2 + i\, 2\, \zeta_m\, \omega_m\, \omega} \right] \right\} \tag{14}$$

where ψ_{qm} is the force (or moment) at location q and mode m. The expression for total response force (or moment) at location q due to the entire pressure field is similar to that for acceleration in (11):

$$F_q(\omega) = \left[\mathrm{H}_{f_q} \sqrt{\mathbf{W}} \ \Gamma \sqrt{\mathbf{W}} \ \mathrm{H}_{f_q}^\dagger \right] P_{ref} \tag{15}$$

where $F_q(\omega)$ is the force PSD at location q, and $\mathrm{H}_{f_q}(\omega) = \left[H_{f_q/p_1} \quad H_{f_q/p_2} \quad \cdots \quad H_{f_q/p_{N_p}} \right]$.

The term inside the bracket in eq (15) may be considered the squared transfer function between the total interface force at location q, and the entire diffuse pressure field:

$$\left| H_{f_q/p}(\omega) \right|^2 = \mathrm{H}_{f_q} \sqrt{\mathbf{W}} \ \Gamma \sqrt{\mathbf{W}} \ \mathrm{H}_{f_q}^\dagger = \frac{F_q(\omega)}{P_{ref}(\omega)} \tag{16}$$

Again, the weighting functions $\mathbf{W}$ may be dropped for spatially uniform pressure autospectra.

The linear components of the stress and strain tensors at location j may also be determined using eqs (14) - (16) by replacing the modal forces ψ_{qm} with the modal stresses φ_{jm} and strains ξ_{jm}, respectively.

All of the modal data required to implement eqs (11) and (15) for acceleration, force, moment, stress and strain responses are obtained from any general purpose finite element code such as NASTRAN (SOL 103). A static solver such as NASTRAN (SOL 101) may be used to obtain the static force distribution corresponding to a unit pressure on each patch. In summary, the data required to implement the RPTF method for all response types are the following:

Modal Data:

$\omega = [\omega_1 \quad \omega_2 \quad \cdots \quad \omega_M]$ - natural frequencies for modes $1 - M$ of bare skin,

$\Phi_j = \begin{bmatrix} \phi_{j1} & \phi_{j2} & \cdots & \phi_{jM} \end{bmatrix}$ - mode shapes for loaded skin at a few reference locations j,

$\Psi_q = \begin{bmatrix} \psi_{q1} & \psi_{q2} & \cdots & \psi_{qM} \end{bmatrix}$ - modal interface forces for loaded skin at locations q,

$\boldsymbol{\varphi}_j = \begin{bmatrix} \varphi_{j1} & \varphi_{j2} & \cdots & \varphi_{jM} \end{bmatrix}$ - modal stresses for loaded skin at locations j,

$\boldsymbol{\xi}_j = \begin{bmatrix} \xi_{j1} & \xi_{j2} & \cdots & \xi_{jM} \end{bmatrix}$ - modal strains for loaded skin at locations j.

Static Data:

$F_b = [F_{b1} \quad F_{b2} \quad \cdots \quad F_{bN_b}]$,
$b = 1, 2, ... N_p$
- force distributions on nodes for unit pressure on patches b,

$R_{bc} = \sqrt{(x_b - x_c)^2 + (y_b - y_c)^2 + (z_b - z_c)^2}$ - distance between area centroids of patches b and c.

Pressure Data:

$P_{ref}(\omega)$ - reference pressure autospectrum.

$W_{bb}(\omega)$ - scaling functions for non-uniform pressure autospectra over the entire skin. These may coincide with assigned "zone" autospectra for a specific launch vehicle. That is, use the same W_{bb} on patches within specified launch vehicle zones. Set W_{bb} to unity if unknown.

ANALYSIS RESULTS

TYPICAL ACCELERATION RESPONSE

A program was developed using Matlab to implement the foregoing theoretical discussion for the curved orthogrid panel responses. Selected examples of the vast body of predicted response data are presented to illustrate the methodology. In Figure 8, four accelerometer locations were chosen for comparing the test and analysis results. The directions associated with each triax are designated "Z" (normal to panel), "H" (panel hoop), and "A" (panel axial). Triaxes 11 and 22 were located on the panel at orthogrid junctions near two of the four component mounting brackets. Triax 13 was located on the primary component plate, directly above the mounting bracket near Triax 11. Triax 15 was located near the center of the primary component plate. We have focused on the acceleration, velocity and displacement response comparisons between predicted and measured at locations 11 and 15 in this paper.

The autospectral densities of acceleration normal to the panel (Z) at location 11 are compared in Figure 9 for the unloaded panel (Configuration ES-E6-P15-WUL) and the loaded panel with the heaviest mockup component weight (Configuration ES-E6-P15-W3). Excellent correspondence between the predicted and measured responses is observed for both configurations. This result was typical of all of the acceleration responses examined in this study. A slight upward shift in the predicted frequency of the first major response peak was observed near 100 Hz and 65 Hz for the unloaded and loaded configurations respectively. This shift was attributed to the slightly stiffer boundary conditions used in the model, as described earlier. Higher frequency responses did not exhibit this shift, indicating that higher modes are insensitive to the attachment conditions at the panel perimeter. The predicted responses at frequencies higher than approximately 1100 Hz were observed to roll off sooner than measured, possibly indicating a need for higher patch densities, i.e., greater than 225 pressure patches for these cases.

The autospectral densities of acceleration in all three directions at location 15 are compared in Figure 10 for a loaded panel with one increment plate (Configuration ES-E2-P10-W1). Good agreement between predicted and measured responses is again observed. If not for the appearance of noise floor from the measurement system which affects the axial response below 200 Hz at location 15, the comparison would be even better. One of the most satisfying indicators that the methodology works is that the results compare well for different configurations of the model and hardware. At frequencies higher than approximately 900 Hz, the predictions in the two tangential directions (hoop and axial) drop relative to the measured, possibly indicating a need for either higher patch or mesh densities, i.e., greater than 100 patches or four elements/cell respectively for these directions. The measured and predicted responses beyond 900 Hz are much closer in the normal direction, with slightly higher roll off in the prediction than measured. The measured response in the axial direction below 100 Hz was expected to roll off in a fashion similar to the prediction; the test anomaly has not been resolved and is being investigated. In any case, the most important response occurs in the normal direction, the primary driver for strain and fatigue damage. The test article is much more responsive in certain directions than others; poor tracking below 200 Hz in the axial direction may be explained by the presence of a measurement system noise floor.
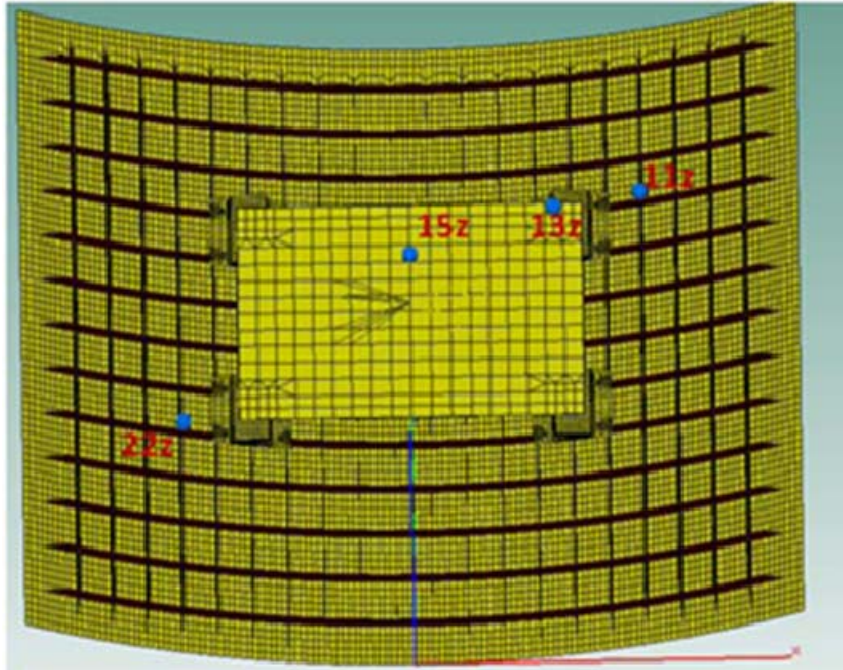
Figure 8. Four locations chosen for comparing measured with predicted acceleration responses
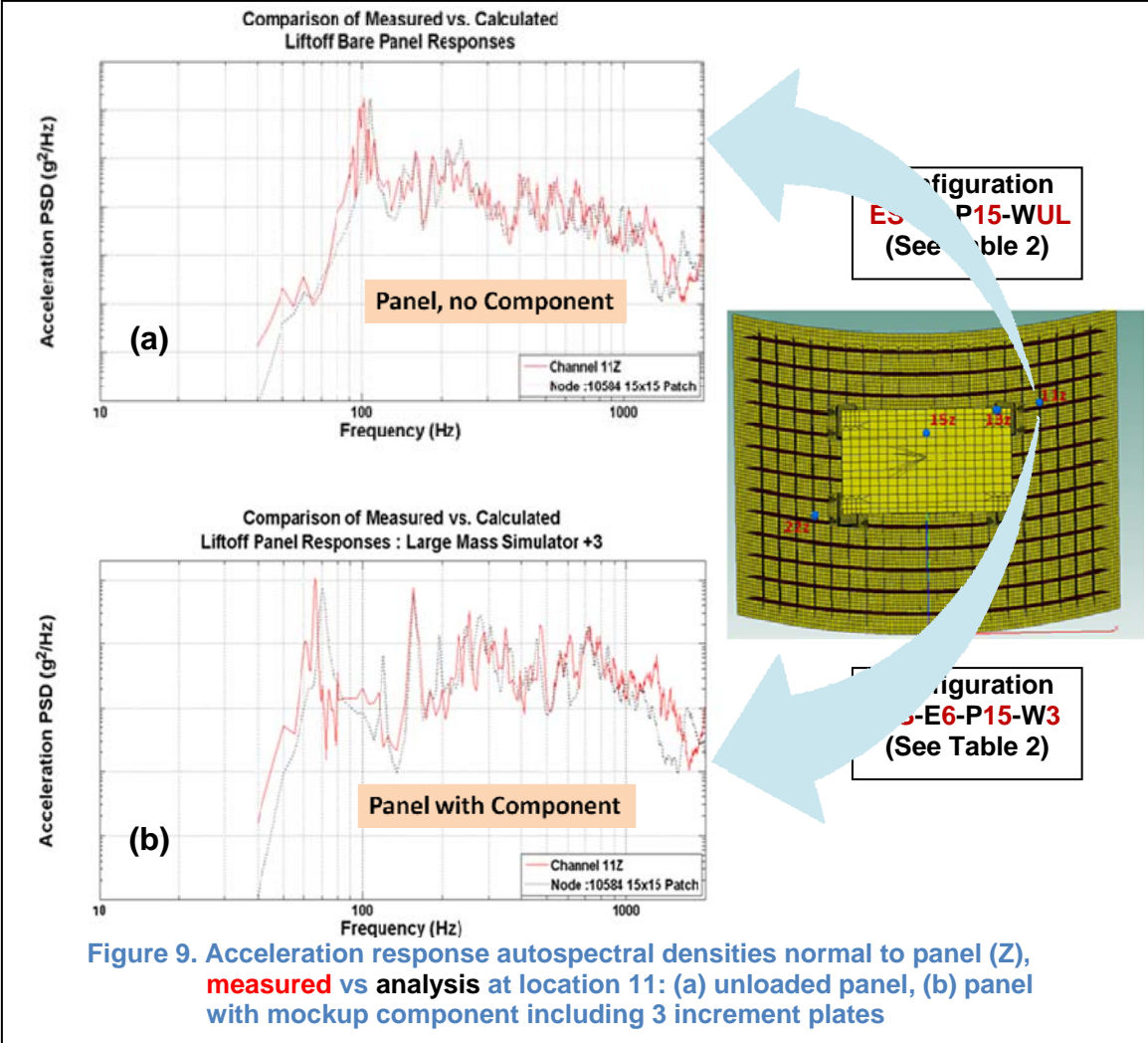
Figure 9. Acceleration response autospectral densities normal to panel (Z), measured vs analysis at location 11: (a) unloaded panel, (b) panel with mockup component including 3 increment plates

Figure 10. Acceleration response autospectral densities in hoop, axial and normal directions, measured vs analysis at location 15, with mockup component including 1 increment plate
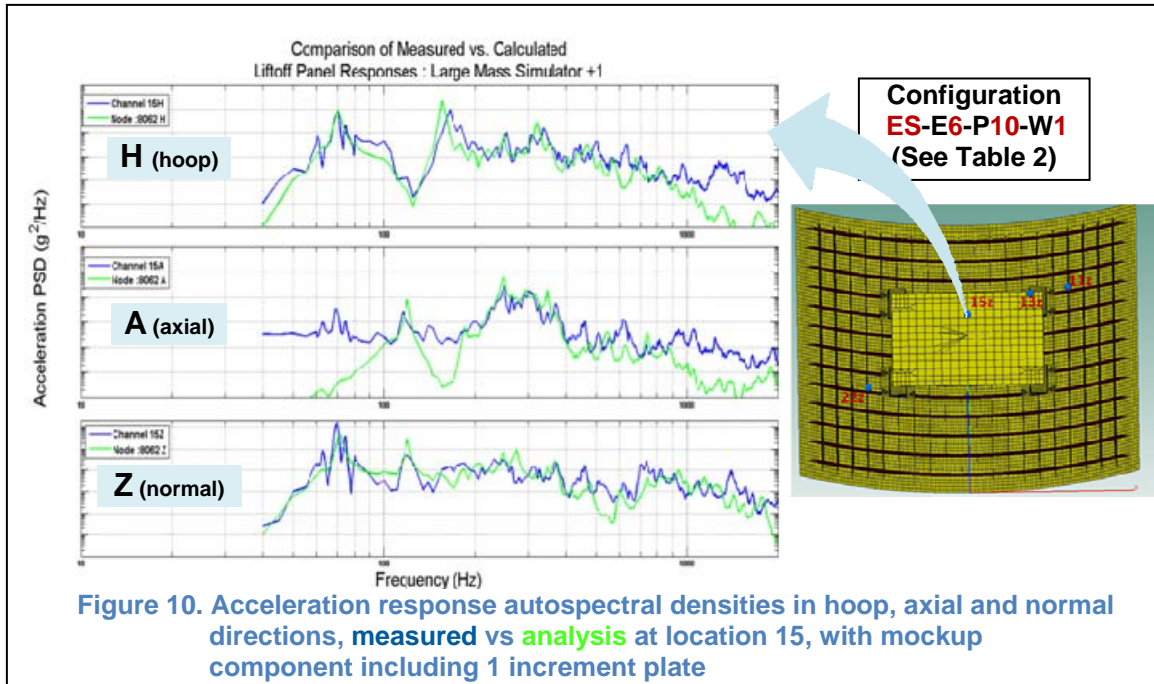
TYPICAL STRAIN RESPONSE

The Matlab program used to compute the acceleration was also used for the strain response. The linear components of the strain tensor at any gage location j were determined using eqs (14) - (16), replacing the modal forces ψ_{qm} with the modal strains ξ_{jm} respectively. In Figure 11, six rosette strain gage locations, all on the face of an orthogrid rib, were chosen for comparing the test and analysis results. Due to the volume of data, the only strain location discussed in this presentation is gage 10 near the triaxial accelerometer at location 11. The strain results at other locations were similar. The two perpendicular axes of each 3-channel rosette were aligned with the panel normal (Z) and the direction of the rib axis (H or A). Gage 10 is mounted on a vertical rib. Hence, the strains for location 10 were measured on the rib in directions normal to the panel (Z) and parallel to the panel vertical axis (A).
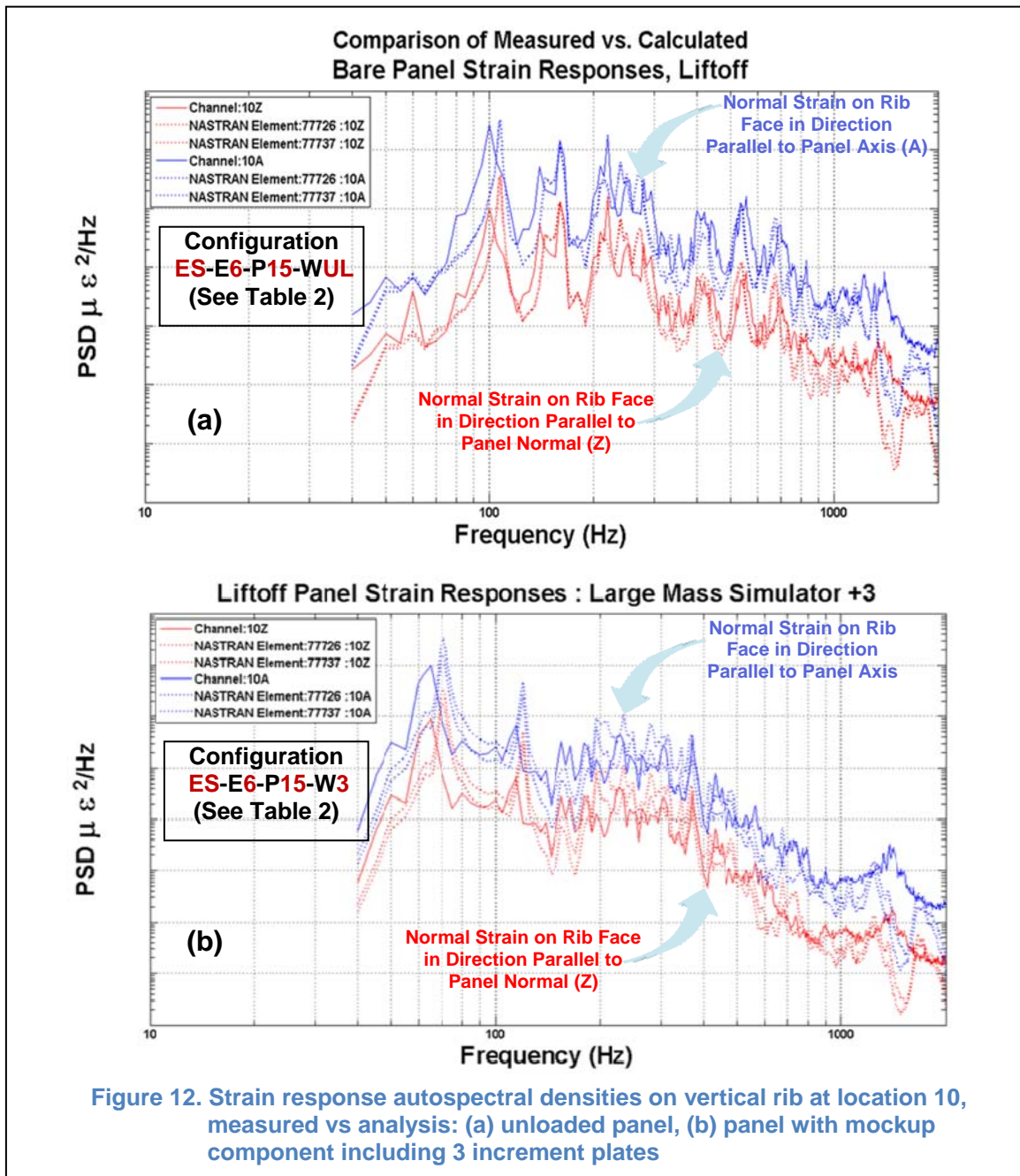
The autospectral densities of strain in the two directions on the rib face at location 10 are compared in Figure 12 for the unloaded panel (Configuration ES-E6-P15-WUL) and the loaded panel with the heaviest component weight (Configuration ES-E6-P15-W3). Again, good correspondence between the predicted and measured responses was observed for both configurations. This result was typical of all of the strain responses examined in this study. The same slight upward shift in the predicted frequency of the first major peak observed in the acceleration response was also detected in the strain response near 100 Hz and 65 Hz for the unloaded and loaded configurations respectively. Beyond 1100 Hz, the predicted strains rolled off more quickly than the measured strains, as observed earlier in the comparison of accelerations. Again, this steeper roll off after 1100 Hz may indicate a need for greater patch density to adequately capture the strains at these frequencies.

Figure 11. Six locations chosen for comparing measured with predicted strain responses
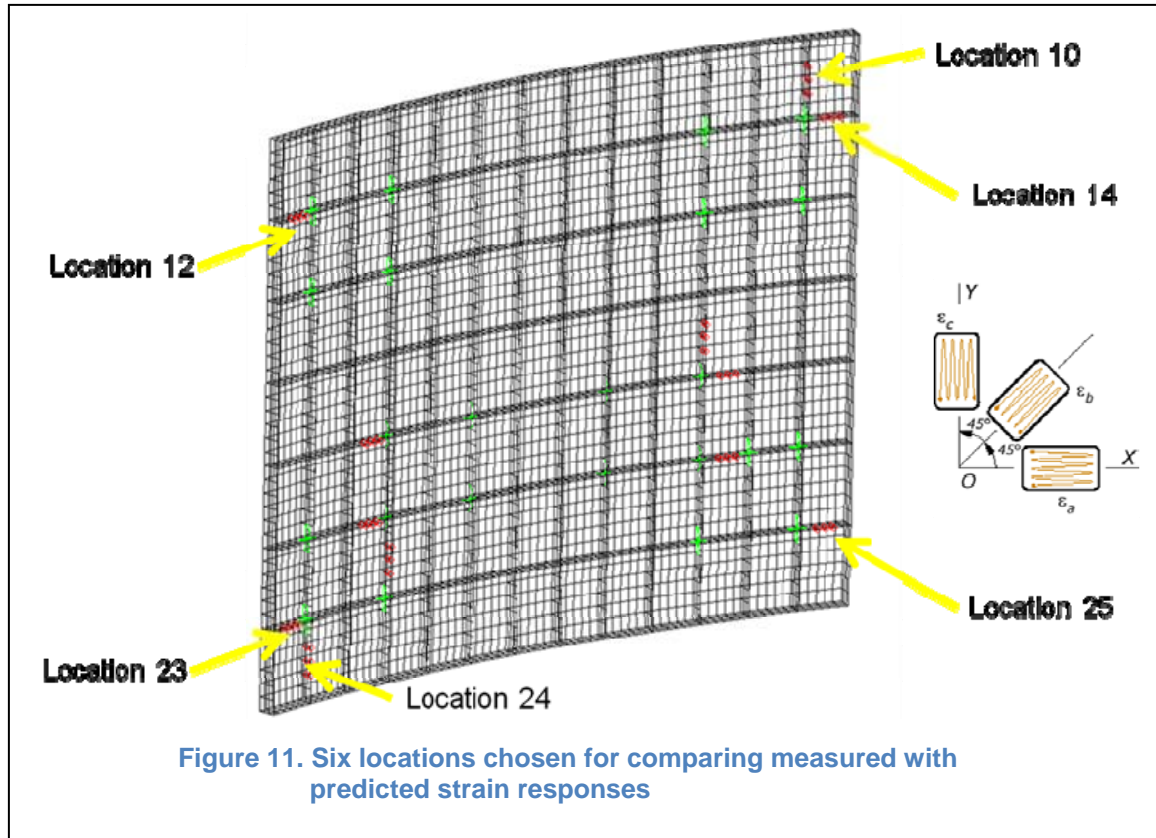
CUMULATIVE ROOT MEAN SQUARE RESPONSES

Because the model predictions were often observed to diverge from the measurements at a threshold frequency near 1000 Hz, a method for determining the appropriate frequency band to use for purposes of design and test development was desired. Since structural performance is most often assessed using strain to evaluate either low or high cycle fatigue life, the key consideration was to determine the response frequency beyond which no significant RMS strain was observed to accumulate. Interface forces between the component and the panel were also of significant interest. Since strain gages and load cells are used infrequently to measure response during qualification testing, a second objective was to observe any strong correlation between dynamic strain or interface force and acceleration, velocity or displacement.

In Figure 13, the RMS values of all five response metrics (strain, interface force, acceleration, velocity and displacement), normalized to unity for the purpose of comparison, were accumulated over the full measurement frequency range. The integration of the spectral density response was performed over frequency, the square root of which is the RMS value of each response. A strong correlation of strain and interface force with velocity is easily discerned in Figure 13, with a threshold frequency below 900 Hz. Above this threshold, very little additional RMS is accumulated. Therefore a consideration of the convergence of RMS velocity is a good indicator of the upper frequency limit needed for estimating component/panel interface force and panel stress and strain. Contrast the convergence of RMS velocity (and strain) with that of acceleration, which may have converged by 2000 Hz or higher. Thus, while acceleration may appear to be significant between 1000 and 2000 Hz, it may cause no additional stress in the system. Qualification testing based on this result may be adequate for assessing safety margins using half of the full frequency range. On the other hand, a cutoff frequency based on displacement is non-conservative since RMS displacement converges at approximately 300 Hz. From 300 to 900 Hz, significant RMS strain and interface force are accumulated with higher potential for structural damage.

Figure 12. Strain response autospectral densities on vertical rib at location 10, measured vs analysis: (a) unloaded panel, (b) panel with mockup component including 3 increment plates

The data plotted in Figure 13 are summarized in Table 3. Cumulative RMS fractions for acceleration, velocity, displacement, interface force and strain are listed for six frequencies, with the RMS fraction nearest 95% highlighted in red. This manner of presenting the cumulative RMS data emphasizes the similar frequency convergence of velocity, strain and interface force, and the dissimilar convergence of displacement and acceleration.

Figure 14 helps to explain why velocity is such a good indicator for assigning an appropriate frequency cutoff to evaluate strain. The high-frequency roll off of the velocity and strain spectral densities was observed to be nearly the same. In this case *a -12 dB/octave slope*

was plotted for comparison. In contrast, since acceleration is the derivative of velocity, velocity rolls off twice as fast as acceleration (factor of four on the PSDs). Similarly, displacement rolls off twice as fast as velocity. Again the displacement PSD rolls off four times more quickly because PSDs contain a square.

The correlation of strain and interface force with velocity has previously been explored in the literature. Without further elaboration, the underlying theoretical basis for the phenomenon involves a spatial exchange of kinetic and potential energies during system vibration.
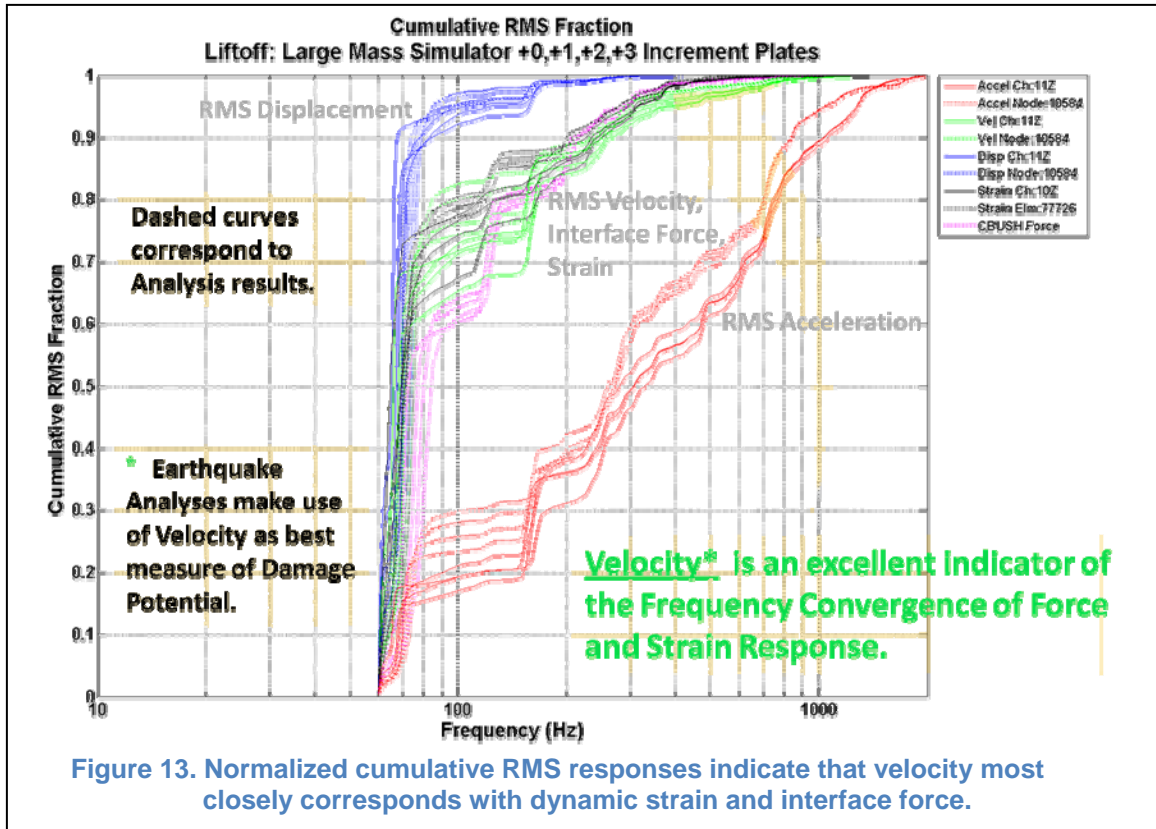

Figure 13. Normalized cumulative RMS responses indicate that velocity most closely corresponds with dynamic strain and interface force.

Table 3. Cumulative RMS Fraction					
Large Mass Simulator +3 increment plates					
Frequency [Hz]	Acceleration (N:10584)	Velocity (N:10584)	Displacement (N:10584)	CBUSH Force (E:800010012)	Strain (E:77726)
100	0.23	0.74	0.95	0.60	0.77
150	0.26	0.77	0.96	0.81	0.86
200	0.39	0.87	0.99	0.86	0.89
250	0.45	0.90	0.99	0.94	0.93
300	0.57	0.95	1.00	0.95	0.96
1015	0.95	1.00	1.00	1.00	1.00

Figure 14. Both strain and velocity PSDs roll off at nearly -12 dB/octave.
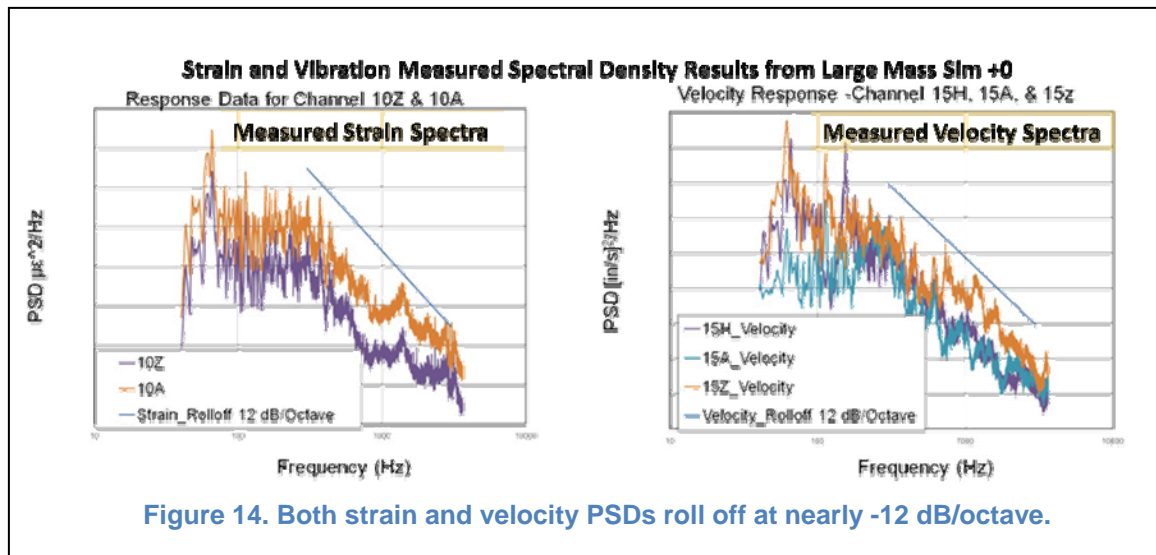
RESPONSE SENSITIVITIES TO MODELING PARAMETERS AND COMPONENT WEIGHT

The focus of the discussion until now has been to establish the predictive capability of the RPTF method. We now examine the degree to which modeling parameters may affect the solution. Several versions of the panel model were created to determine sensitivities to mesh density (3), patch density (30), weight of an attached component (5), and modeling techniques (3) for representing the orthogrid ribs, resulting in 885 different load cases as previously described. The metrics used to evaluate response sensitivities were the PSDs and cumulative RMS values of acceleration, strain and interface force.

Acceleration Response Sensitivities

Acceleration response PSDs and cumulative RMS values were plotted over the range of each modeling parameter and component weight in Figure 15 through Figure 21. Included in each figure are three graphs: (1) response PSD, (2) cumulative RMS value, and (3) a bar chart showing the RMS values for each parameter variation. The presentation is limited to location 11, positioned on an orthgrid rib junction close to one of the four component mounting brackets. This location is typical of those used to develop input vibration environments for panel mounted components.

Figure 15 shows the sensitivity of acceleration to component weight, including a configuration with no mounted component. A dramatic change in the response of the unloaded panel (WUL) was observed when the first 95-lb component was added to the configuration (W0). The addition of up to 3 additional 15-lb increment plates on top of the primary component plate had little effect on the response. The effect of Barrett mass attenuation on the unloaded panel is easily observed when a component is added. A downward shift in the primary mode frequencies, and a re-distribution of the mass participation of all the modes dropped the RMS value several decibels. Most of the change was due to the frequency drop of the first primary mode near 104 Hz to about 73 Hz, with lower peak response at the latter. The shape of the input sound spectrum was relatively flat over this range, so the decrease in peak magnitude was solely attributed to the change in system dynamic characteristics. Note that the dominant peak of the unloaded panel near 104 Hz became a non-responsive node with the added component.

Because the accelerations were found to be insensitive to the addition of the 15-lb increment plates, further presentations of the response data only include the unloaded panel (WUL) and loaded panel with the highest weight (W3).

Figure 15. Acceleration PSD and RMS sensitivities to *component weight*
Configurations ES-E6-P30-WUL, ES-E6-P30-W0, ES-E6-P30-W1, ES-E6-P30-W2, ES-E6-P30-W3
(***All mockup component weights***, shell ribs, high mesh density, high patch density)
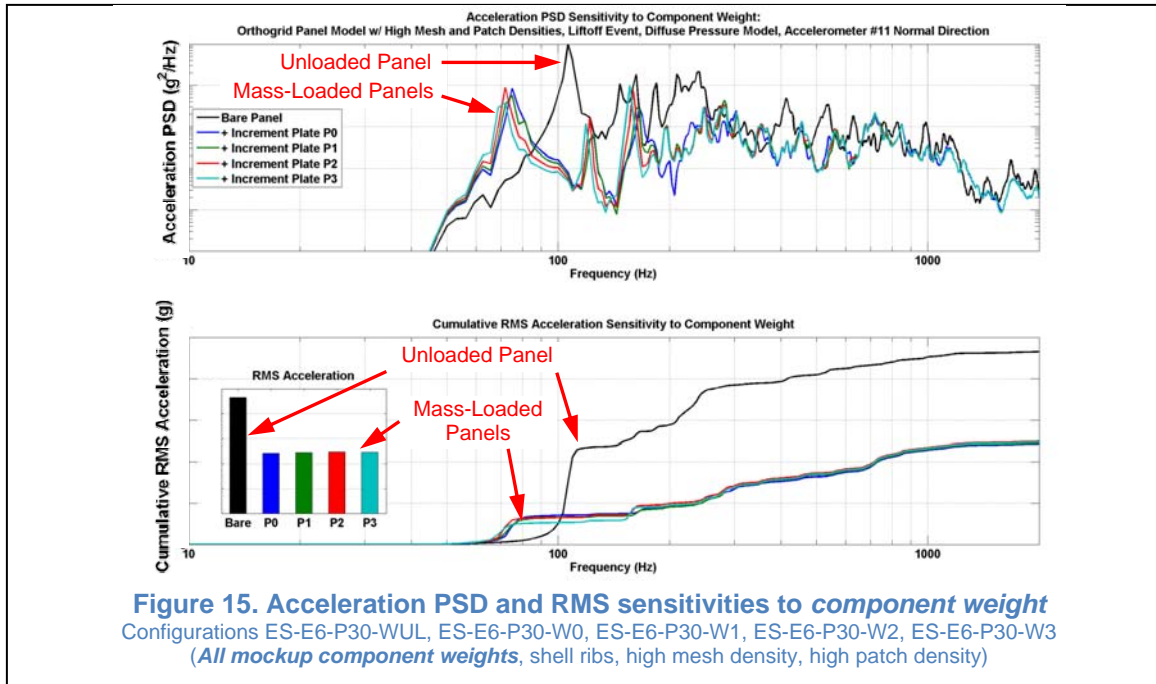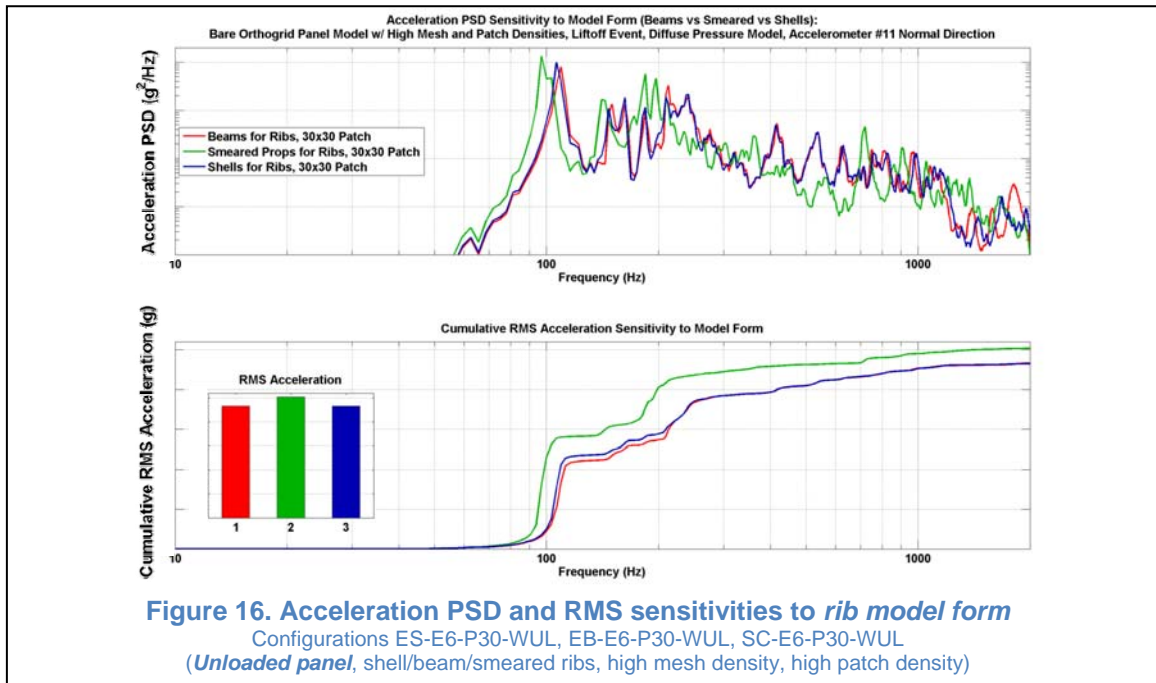
Figure 16 (unloaded panel) and Figure 17 (loaded panel) show the sensitivity of acceleration to the three techniques for modeling the orthogrid ribs. Although less pronounced in the loaded configuration, both figures indicate that the smeared property technique does not track as well with the explicit shell and beam methods of rib representation. Although the technique remains viable, this approach may require adjustment or optimization to perform as well as the other two. The two explicit techniques match closely, indicating either method may be used. Of the two explicit techniques, beams are preferred for computational efficiency, although shells may be required if dynamic stresses in the ribs are important to a particular design problem.

Figure 16. Acceleration PSD and RMS sensitivities to *rib model form*
Configurations ES-E6-P30-WUL, EB-E6-P30-WUL, SC-E6-P30-WUL
(***Unloaded panel***, shell/beam/smeared ribs, high mesh density, high patch density)

Figure 17. Acceleration PSD and RMS sensitivities to *rib model form*
Configurations ES-E6-P30-W3, EB-E6-P30-W3, SC-E6-P30-W3
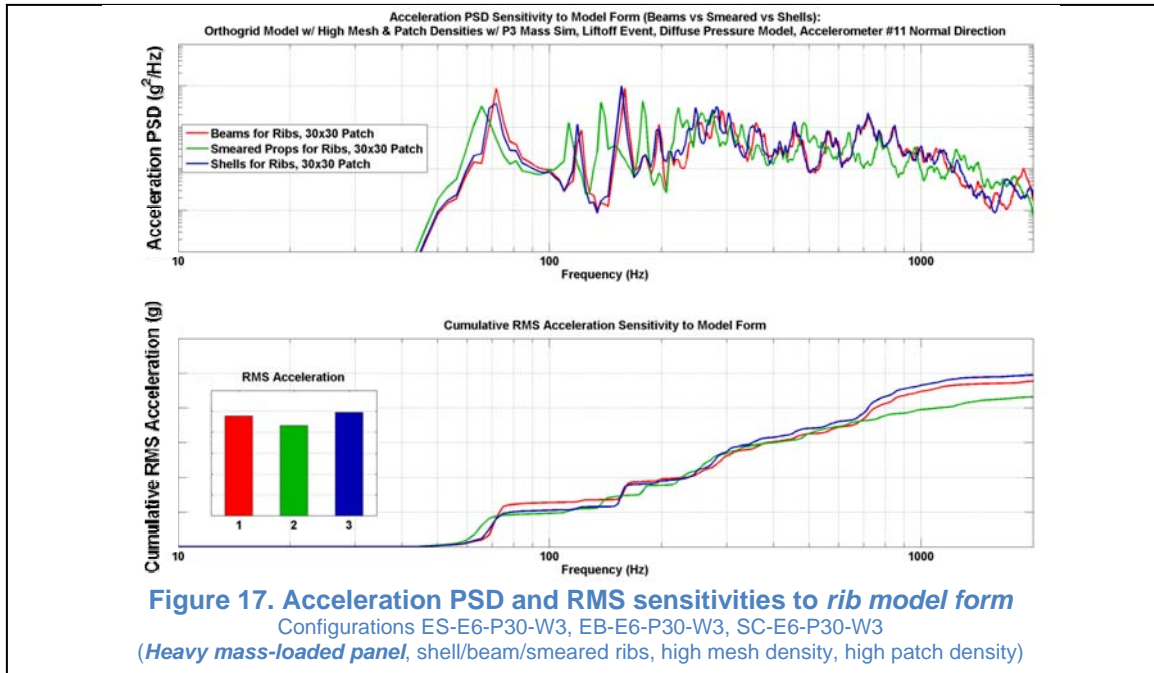(***Heavy mass-loaded panel***, shell/beam/smeared ribs, high mesh density, high patch density)

Figure 18 (unloaded panel) and Figure 19 (loaded panel) show the sensitivity of acceleration to mesh density. The three mesh densities with one, four and thirty-six elements per orthogrid cell compared favorably in the frequency range of interest for loads and strain. Minor differences were observed for the coarsest mesh in the unloaded panel starting at about 400 Hz. Slightly more pronounced differences were observed in the loaded panel for the medium mesh density configuration. This result does not seem congruent, and is currently under investigation. The anomaly may be due to an error in the plot label. Even with these minor variations in the response, a smoothed envelope derived from these results would be quite similar as a vibration design criterion. All three mesh densities explored were considered adequate for the purposes of this study. The rib spacing precluded a coarser mesh with the explicit shell representation of the ribs.
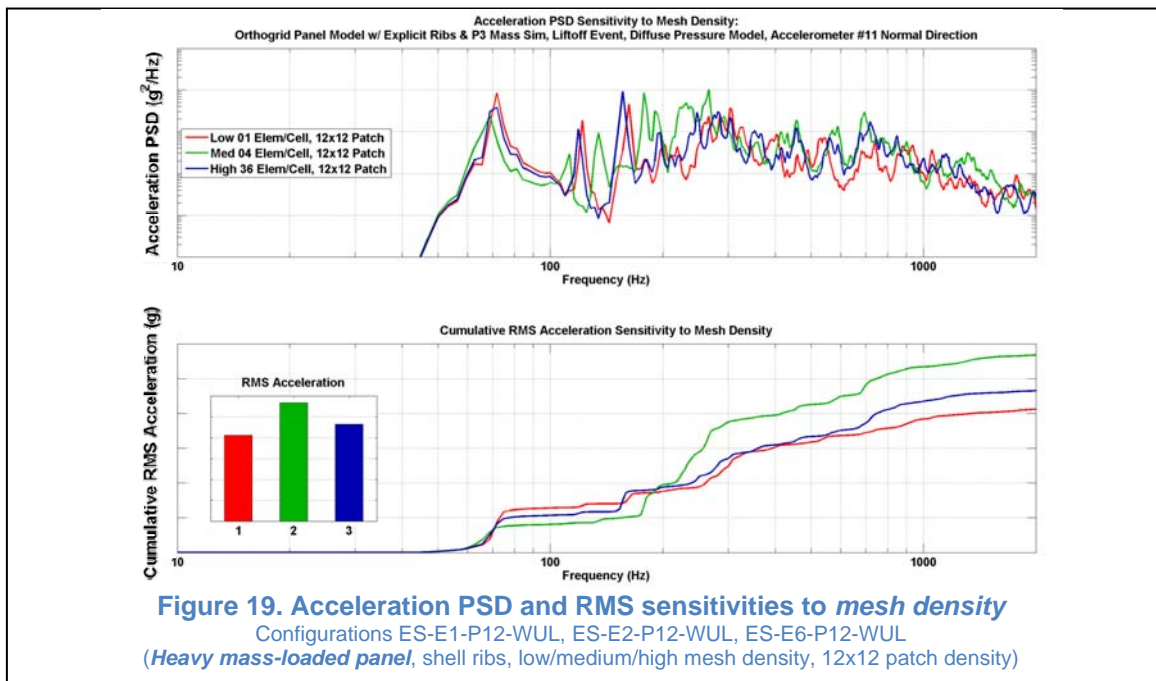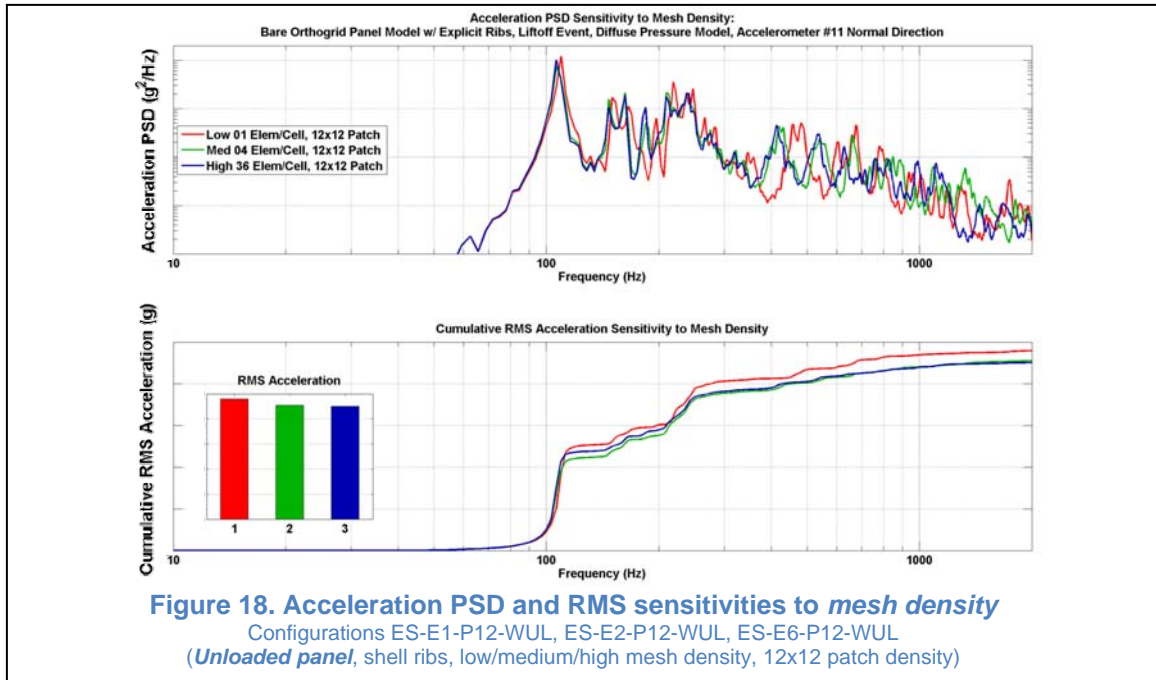
Figure 18. Acceleration PSD and RMS sensitivities to *mesh density*
Configurations ES-E1-P12-WUL, ES-E2-P12-WUL, ES-E6-P12-WUL
(***Unloaded panel***, shell ribs, low/medium/high mesh density, 12x12 patch density)

Figure 19. Acceleration PSD and RMS sensitivities to *mesh density*
Configurations ES-E1-P12-WUL, ES-E2-P12-WUL, ES-E6-P12-WUL
(***Heavy mass-loaded panel***, shell ribs, low/medium/high mesh density, 12x12 patch density)

Figure 20 (unloaded panel) and Figure 21 (loaded panel) show the sensitivity of acceleration to patch density. An adequate patch density for applying the diffuse pressure field is critical for predicting the measured response. In these figures, a total of 29 patch configurations (P02 – P30) were assembled and entered into the RPTF program to compute the responses. The greatest sensitivity to patch density was demonstrated for responses above the fluid/panel coincidence frequency which is approximately 400 Hz for this test article. Convergence of the solution can be seen from below as patch density increases. This is especially true above the coincidence frequency where the waves are said to be acoustically fast. Thus, a general

requirement for accurate model-based acceleration predictions of any panel subjected to diffuse acoustic field is the selection of an adequate patch density, particularly above the coincidence frequency.

Over prediction of the response at low frequencies can also occur when the patch density is too low, as observed in both figures. Over prediction of the acceleration response arises from the fact that applied forces within each patch are perfectly coherent, increasing the probability that coarse patterns with large-area patches may inadvertently and erroneously tune to certain low-frequency modes of the panel. Such a construct, i.e., large-area discretization of the pressure field, does not physically occur in either the laboratory or a real launch environment.

The computational cost can be high for fine patch patterns with high patch density. Furthermore, the frequency range of interest may be significantly lower than the coincidence frequency. Therefore, the goal is to choose a patch density that is adequate for the purpose of the analysis, the structural design and driving environment, but not excessively fine. With recent advances in parallel computing platforms and associated software, the cost of high patch density models will decrease significantly. But knowledge of the minimum requirement for patch assignments is always recommended. If the computational overhead is reasonable, selecting a patch density so that the patch dimensions (or distance from one patch cg to the next) do not exceed ¼ of the wavelength of any structural or acoustic mode below the highest frequency of interest can be adequate for preventing errors in both low and high frequency response predictions.
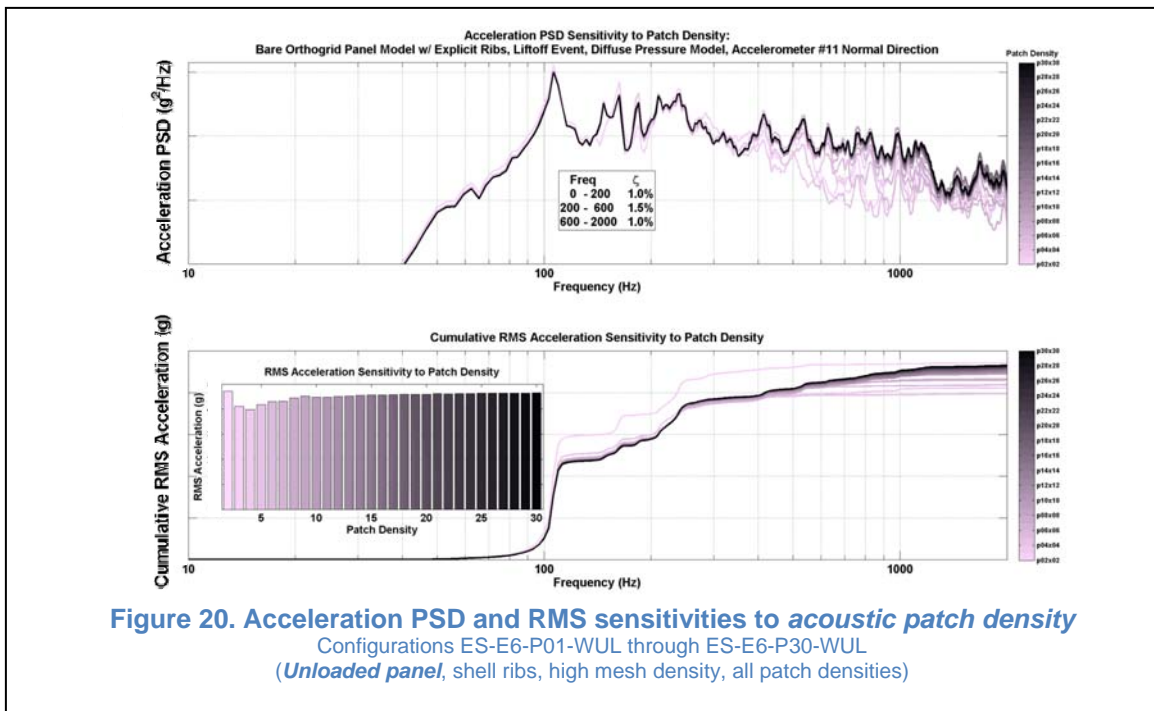

Figure 20. Acceleration PSD and RMS sensitivities to *acoustic patch density*
Configurations ES-E6-P01-WUL through ES-E6-P30-WUL
(***Unloaded panel***, shell ribs, high mesh density, all patch densities)

Figure 21. Acceleration PSD and RMS sensitivities to *acoustic patch density*
Configurations ES-E6-P01-W3 through ES-E6-P30-W3
(***Heavy mass-loaded panel***, shell ribs, high mesh density, all patch densities)
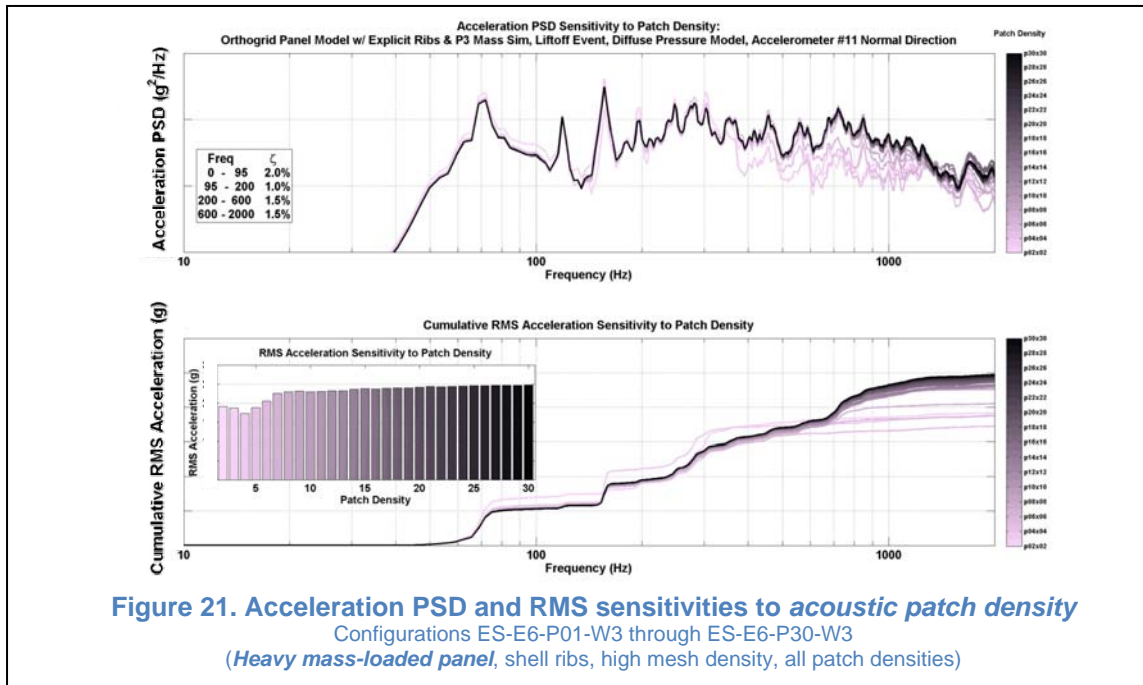
Strain Response Sensitivities

Strain response PSDs and cumulative RMS values were plotted for variations of component weight and patch density in Figure 22 through Figure 24. The presentation is limited to Gage location 10, positioned on an orthgrid rib near Triax location 11. The close proximity of these two instruments was chosen to maximize the observable interaction between velocity and strain.

The foregoing discussion of acceleration response is largely applicable to the strain response with two important exceptions. First, since the roll off in the strain response was shown earlier to be similar to velocity, and since acceleration is the time derivative of velocity, the roll off in the strain PSD is four times faster than acceleration. Second, although the same shift in the primary mode frequencies occurred, the peak amplitude of the strain PSD increased significantly when components were added, as observed in Figure 22. The peak acceleration response of the unloaded panel (WUL) was previously shown to decrease when components were added to the assembly (W0). On the other hand, the RMS values for strain were lower for the mass-loaded configurations. Following this trend, one might expect the peak displacement to increase even more than velocity with components mounted to the panel. Time did not permit confirmation of this expectation, but it is consistent with the behavior of a single-DoF system in which a large mass naturally displaces more than a small mass with all other factors being the same.

The result shown in Figure 22 confirms the well-known fact that without mitigating backup structure in the design, heavy components mounted to a panel can result in significant stress and lower safety margins. Although the spread in response in Figure 22 is most significant between the unloaded panel and all other test article configurations, the strain appears to be slightly more sensitive than acceleration to the additional increment plates. Of course, the log scale can be deceptive, so this aspect requires further investigation.

Because the strain continued to remain relatively insensitive to the addition of the 15-lb increment plates, further presentations of the strain data only include the unloaded panel (WUL) and loaded panel with the highest weight (W3).
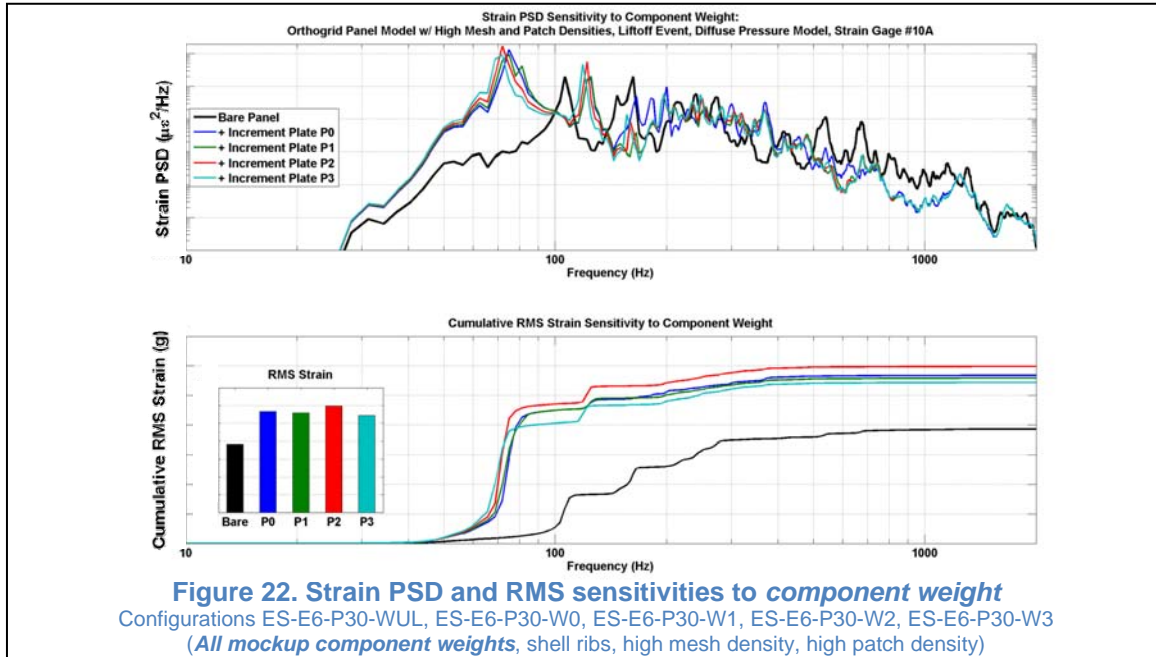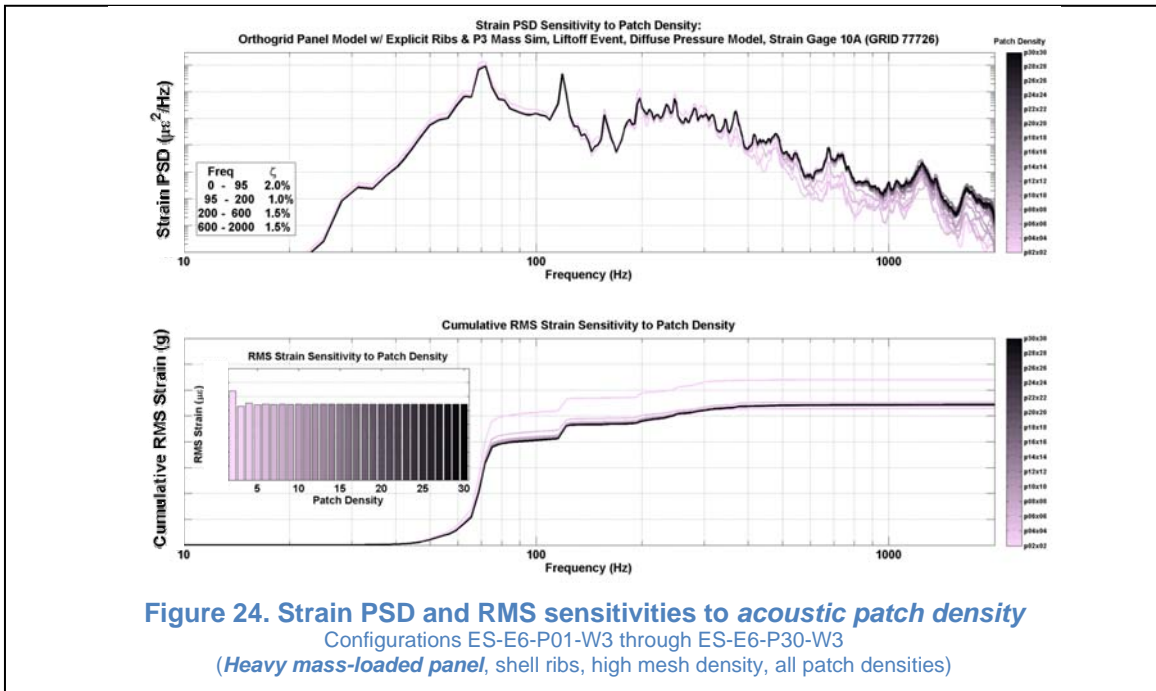

Figure 22. Strain PSD and RMS sensitivities to *component weight*
Configurations ES-E6-P30-WUL, ES-E6-P30-W0, ES-E6-P30-W1, ES-E6-P30-W2, ES-E6-P30-W3
(***All mockup component weights***, shell ribs, high mesh density, high patch density)
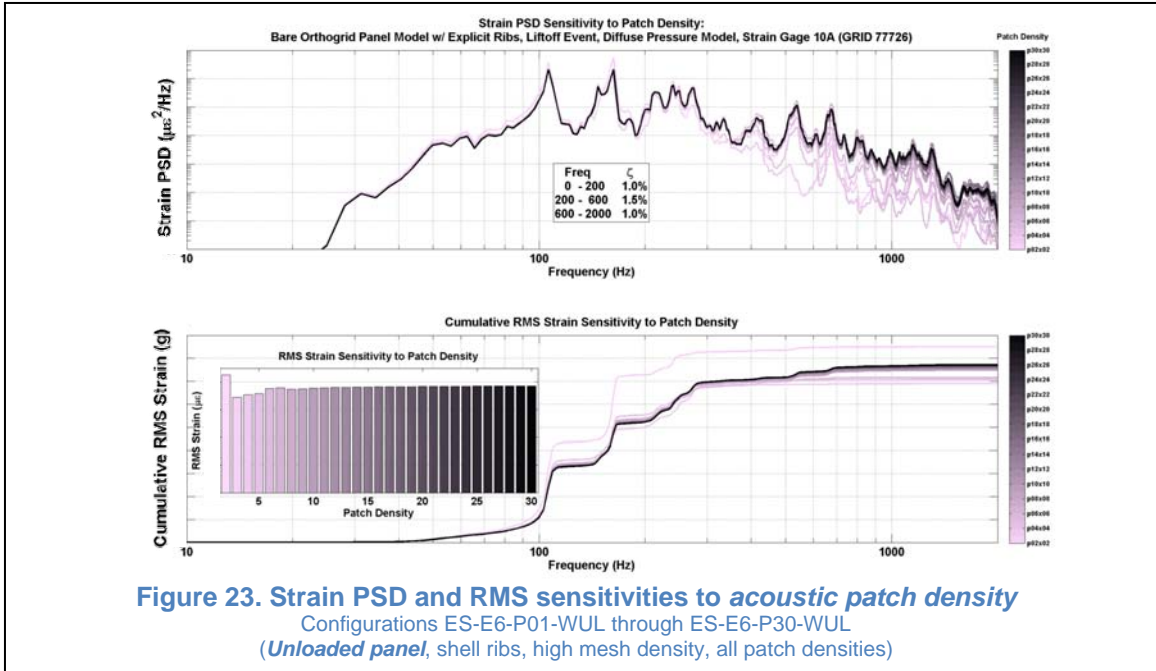
Figure 23 (unloaded panel) and Figure 24 (loaded panel) show the sensitivity of strain to patch density. The foregoing discussion of acceleration sensitivity to patch density is applicable to strain in every respect. However the responses appear to converge with a lower patch density (larger patches) than acceleration, consistent with the greater roll off at higher frequencies. That is, contribution of higher frequency response (requiring smaller patches to adequately capture the dynamics) diminishes more rapidly for strain and velocity than acceleration. Therefore, if the purpose of the analysis is to determine strain levels in the panel, the need for adequate patch density is less critical, and faster turnaround on the analysis may be purchased without significant sacrifice in prediction accuracy.
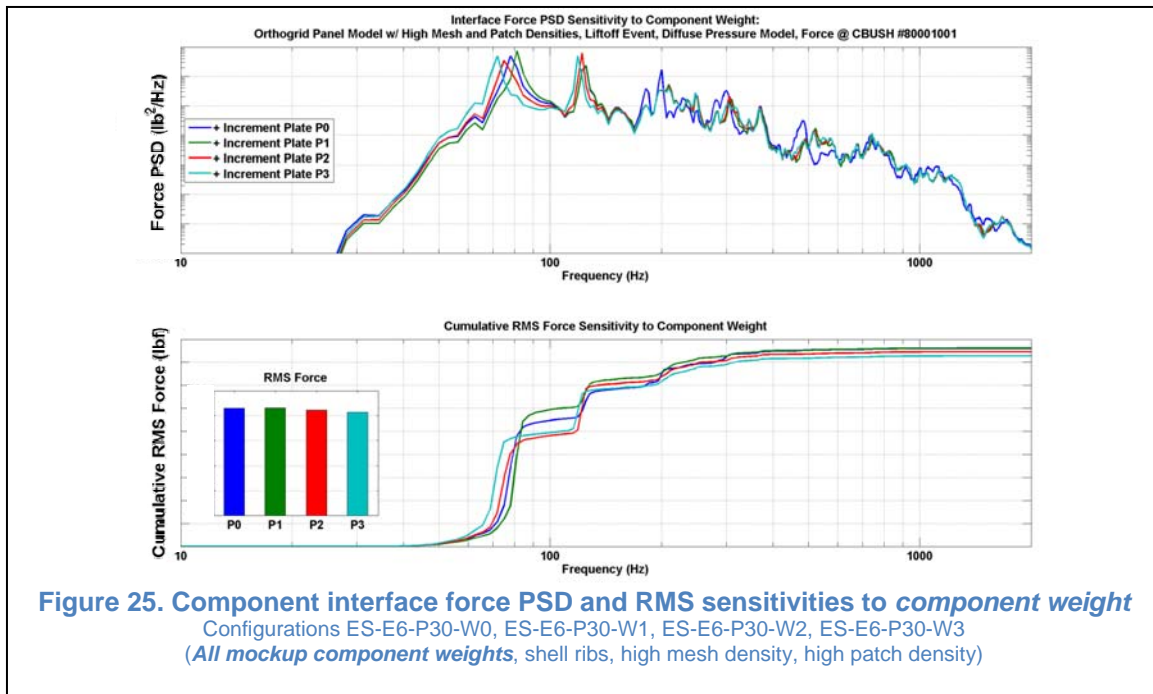
Figure 23. Strain PSD and RMS sensitivities to *acoustic patch density*
Configurations ES-E6-P01-WUL through ES-E6-P30-WUL
(***Unloaded panel***, shell ribs, high mesh density, all patch densities)

Figure 24. Strain PSD and RMS sensitivities to *acoustic patch density*
Configurations ES-E6-P01-W3 through ES-E6-P30-W3
(***Heavy mass-loaded panel***, shell ribs, high mesh density, all patch densities)

Interface Force Response Sensitivities

Although force responses were not measured at the interface between the panel and component hardware, confidence in the force predictions was bolstered by the successful comparisons of measured and predicted acceleration and strain. Since component interface force is often an important factor in the development of test specifications and hardware design, knowledge of the sensitivities to all of the modeling parameters was desirable. Since interface

force has no meaning for the unloaded panel, only the mass-loaded configurations were applicable to the study of interface force.

Force response PSDs and cumulative RMS values at the interface were computed using RPTF and plotted for all variations of modeling parameters and component weight in Figure 25 through Figure 31. The presentation is limited to the CBUSH spring element connecting the panel to the primary plate near Gage location 10 and Triax location 11 described previously.

The foregoing discussions of acceleration and strain responses are entirely applicable to the observed interface response. Since interface force was previously shown to vary with velocity, as did strain, no new relevant aspects of the force response were obtained. The force sensitivity results are included for completeness, but no further discussion is warranted. One small difference observed in the force sensitivity to patch density was that no low frequency error due to low patch density was detectable. In all other respects the previous discussion may be applied to interface force.
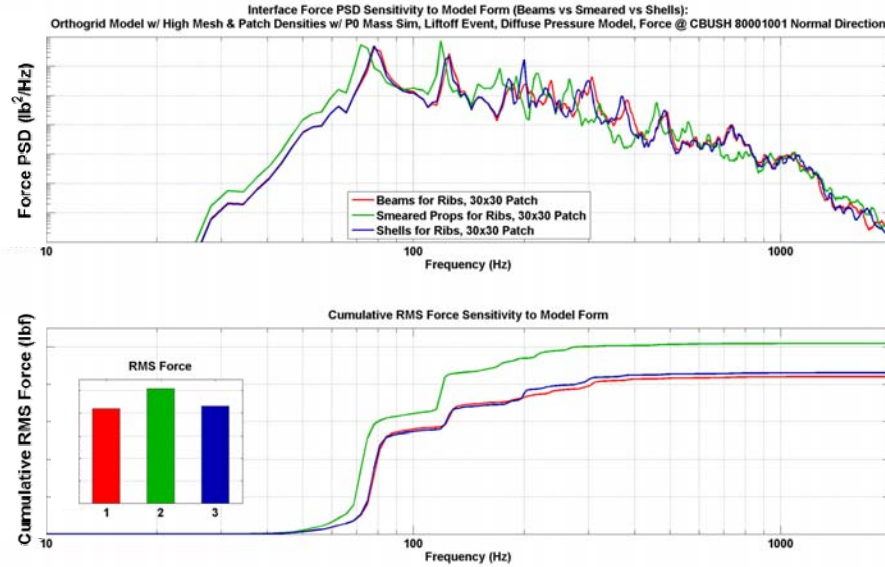

Figure 25. Component interface force PSD and RMS sensitivities to *component weight*
Configurations ES-E6-P30-W0, ES-E6-P30-W1, ES-E6-P30-W2, ES-E6-P30-W3
(***All mockup component weights***, shell ribs, high mesh density, high patch density)

Figure 26. Component interface force PSD and RMS sensitivities to *rib model form*
Configurations ES-E6-P30-W0, EB-E6-P30-W0, SC-E6-P30-W0
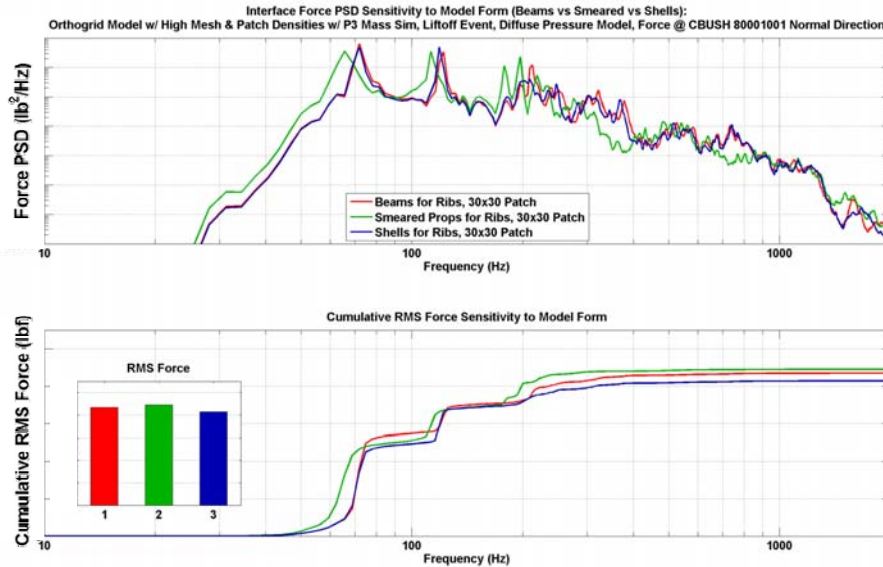(*Light mass-loaded panel*, shell/beam/smeared ribs, high mesh density, high patch density)

Figure 27. Component interface force PSD and RMS sensitivities to *rib model form*
Configurations ES-E6-P30-W3, EB-E6-P30-W3, SC-E6-P30-W3
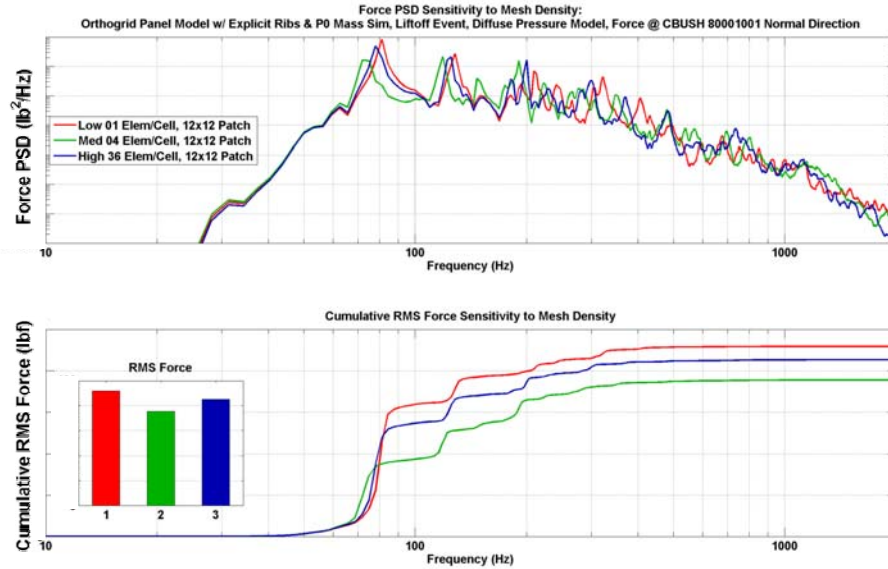(*Heavy mass-loaded panel*, shell/beam/smeared ribs, high mesh density, high patch density)

Figure 28. Component interface force PSD and RMS sensitivities to *mesh density*
Configurations ES-E1-P12-W0, ES-E2-P12-W0, ES-E6-P12-W0
(***Light mass-loaded panel***, shell ribs, low/medium/high mesh density, 12x12 patch density)
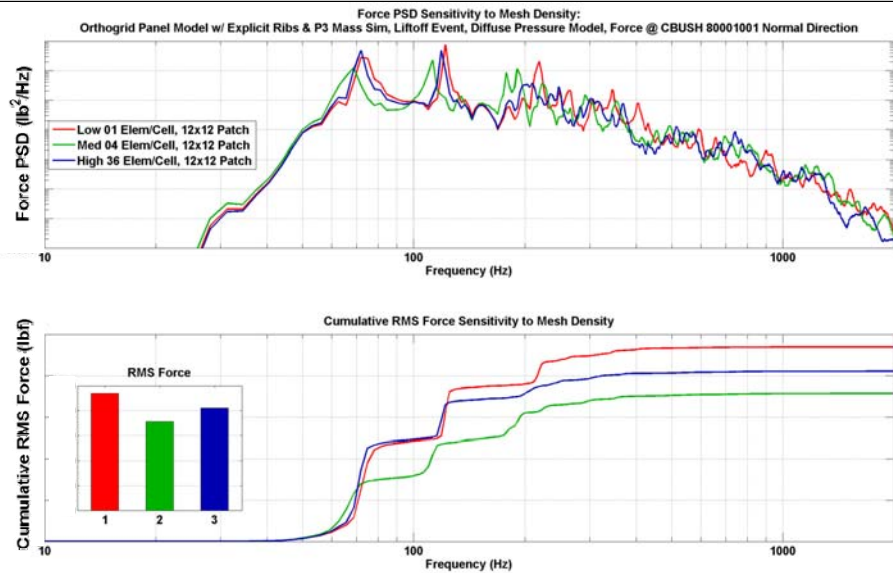

Figure 29. Component interface force PSD and RMS sensitivities to *mesh density*
Configurations ES-E1-P12-W3, ES-E2-P12-W3, ES-E6-P12-W3
(***Heavy mass-loaded panel***, shell ribs, low/medium/high mesh density, 12x12 patch density)

Figure 30. Component interface force PSD and RMS sensitivities to *acoustic patch density*
Configurations ES-E6-P01-W0 through ES-E6-P30-W0
(*Light mass-loaded panel*, shell ribs, high mesh density, all patch densities)

Figure 31. Component interface force PSD and RMS sensitivities to *acoustic patch density*
Configurations ES-E6-P01-W3 through ES-E6-P30-W3
(*Heavy mass-loaded panel*, shell ribs, high mesh density, all patch densities)
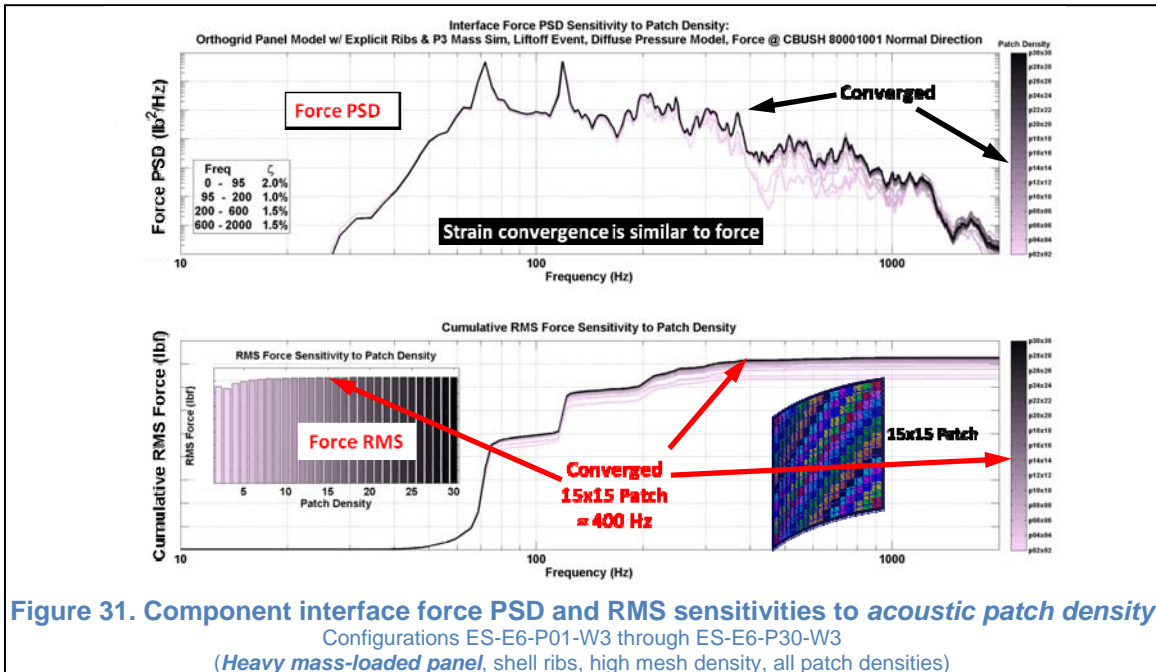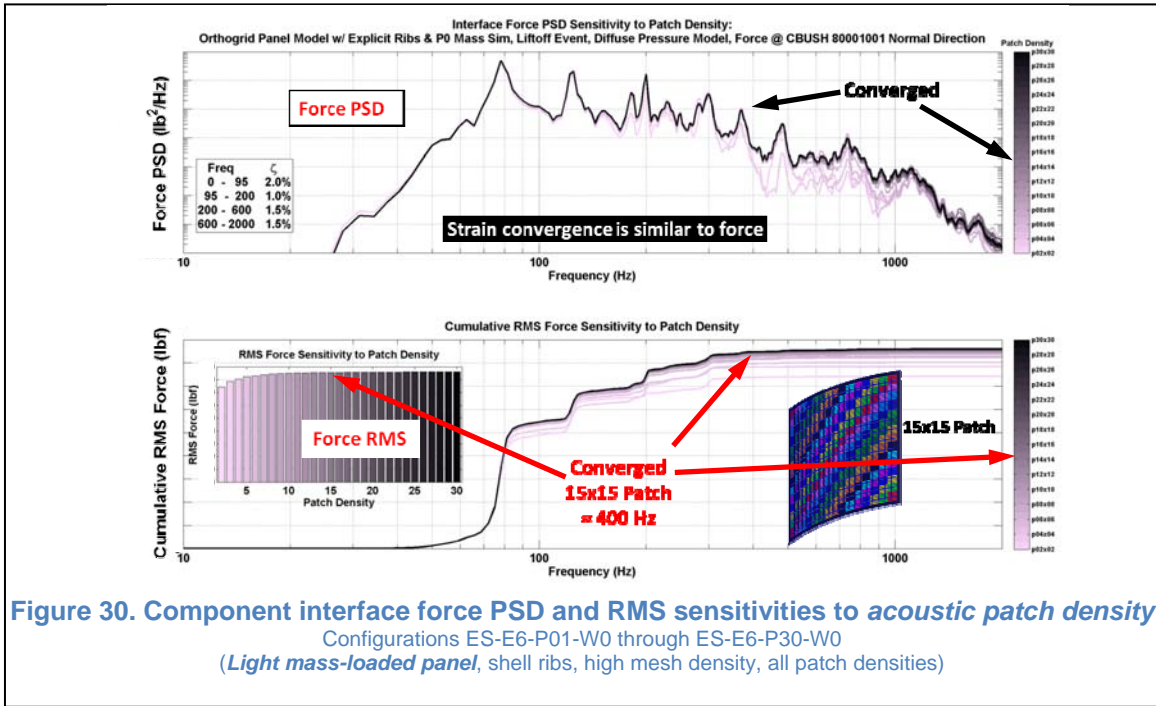
SUMMARY AND CONCLUSIONS

The early sections of this paper provide evidence that the models and approach used to analytically predict the structural vibration response to acoustic-borne energies in a ground test performed admirably. Furthermore the robustness of the approach was demonstrated with suitable predictions for five different configurations of the test article.

The analytical response predictions were verified for both acceleration and strain measurements. The ground test facility, experimental set up and the test articles were described. Additional data was provided showing excellent test/analysis mode correlation from tap modal tests on the hardware mounted in the ground test facility.

Additionally, the authors explored a method to determine the appropriate frequency range required to accurately assess component interface forces, strains and stresses. The velocity spectral density was found to be a better indicator of the threshold frequency for component loads and panel strains than either displacement or acceleration spectral densities. The cumulative RMS value of the velocity spectral density was found to converge at about the same frequency as the interface force and strain responses.

After demonstrating the adequacy of the models and the prediction methodology in the first half of this paper, the focus was shifted to using the models and methodology to assess vibration response sensitivities to one test (component weight) and several analysis parameters, including model mesh density, acoustic patch density and rib modeling techniques (model form).

Although mesh density and model form were among the parameters explored, the analysis showed the responses to be significantly more sensitive to patch density. The analysis was completed for a large number of parameter combinations (885). The configurations included combinations of thirty patch densities, three mesh densities, three techniques for representing the orthogrid ribs, and five test article component weights.

Response sensitivities to patch density verified that inclusion of spatial correlation of the energizing pressure field is important. Inclusion of the cross spectral terms accounts for the energetic responses observed (measured) at the panel coincidence frequency. The responses at frequencies above coincidence are also more energetic when the patch density is fine enough to adequately represent the spatial correlation of the fluid sound pressure wave lengths. The frequency range above the coincidence frequency is said to be acoustically fast.

REFERENCES

1. Rafaely, Boaz, "Spatial-temporal Correlation of a Diffuse Sound Field," J. Acoust. Soc. Am. 107 (6) (June 2000).
2. Maasha, R., Towner, R., LaVerde B., Band, J., "Preliminary Correlation Results Summary for Mass-loaded Vehicle Panel Test Article Finite Element Models and Modal Survey Tests," Proceedings of 2011 Spacecraft and Launch Vehicle Dynamic Environments Workshop, June 2011.
3. MSC.Software Corporation, MSC.NASTRAN 2008 User's Guide, 2008.
4. MathWorks Inc., MATLAB Users Guide, 2010.
5. Craig, Roy, Structural Dynamics, An Introduction to Computer Methods, 1st ed., John Wiley & Sons, NY, 1981.
6. Chung, Y.T., "FEM Validation of Response Matching Method Final Report," HDC-ARRA-8C-026, The Boeing Company, February 24, 2011.
7. Bendat, Julius and Piersol, Allan, Random Data Analysis and Measurement Procedures, 2nd ed., John Wiley & Sons, NY, 1986.
8. Peck, Smith, Fulcher, LaVerde & Hunt, "Development of Component Interface Loads on a Cylindrical Orthogrid Vehicle Section from Test-Correlated Models of a Curved Panel," Slide presentation at the Spacecraft & Launch Vehicle Dynamic Environments 2011 Workshop, The Aerospace Corp., El Segundo, CA, June 7-9, 2011.

9. Blevins, R., "Formulas for Natural Frequency and Mode Shape," Robert E. Krieger Publishing Co., 1979.
10. Blelloch, P., "Predicting Vibro-Acoustic Environments for Aerospace Structures," ATA Engineering, Inc., San Diego CA, November 2010.
11. Blevins, D., Unpublished Drawings, AD01 Acoustic Test Article Hardware, 2010.
12. Braun, S., et al., "Encyclopedia of Vibration," Academic Press, 2002, page 1,265.
13. Archer, J., "Structural Vibration Design," NASA Space Vehicle Design Criteria Monograph Series- NASA SP 8050, June 1970.
14. Harrison, P., LaVerde, B., Teague, D., "Exploring Modeling Options and Conversion of Average Response to Appropriate Vibration Envelopes for a Typical Cylindrical Vehicle Panel with Rib-stiffened Design," Proceeding of 2009 Spacecraft and Launch Vehicle Dynamic Environments Workshop, June 2009.
15. Ferebee, R., "Using the Saturn V and Titan III Vibroacoustic Databanks for Random Vibration Criteria Development," NASA/TM—2009–215902, NASA- MSFC, July 2009.
16. Kaouk, M., Harrison, P., Blelloch, P., "Summary NASA Vibro-Acoustic (VA) Technical Interchange Meeting (TIM)," NASA - Kennedy Space Center, Cape Canaveral, FL October 2009.
17. Kern, D., "Proposal for Reducing Risk Associated with Vibroacoustic Environments" NASA – JPL, California Institute of Technology, Presented at NESC Face To Face, Waco, TX, May 2010.
18. Kelley, A., Harrison, P., Smith, A., et al., "Test Plan - AD01-01 Instrument Unit (IU) and Aft Skirt (AS) Skin Section Acoustic Response Test," CxP Ares-USO-TE-25142, NASA-MSFC, September 2010.
19. Kern, D., et al., "Dynamic Environmental Criteria," NASA-HDBK-7005, National Aeronautics and Space Administration, March 13, 2001.
20. Kolani, A., Scharton, T., Kern, D., "A Review of Mass-Loaded Support Structures Random Vibration Prediction Methodologies," Proceedings of 2010 Spacecraft and Launch Vehicle Dynamic Environments Workshop, June 2010.
21. Grosveld, F., Palumbo, D., et al., "Finite element development of Honeycomb Panel Configurations with Improved Transmission Loss," Proceedings of Internoise Conference, Honolulu, Hawaii, December 3-6, 2006.